2017

Multiscale Modeling of Biological Flow using Lattice Boltzmann Method

Salman Sohrabi
Lehigh University

Multiscale Modeling of Biological Flow using Lattice Boltzmann Method

by

Salman Sohrabi

A Dissertation

Presented to the Graduate and Research Committee

of Lehigh University

in Candidacy for the Degree of

Doctor of Philosophy

in

Mechanical Engineering

Lehigh University

August 2017

Approved and recommended for acceptance as a dissertation.

Salman Sohrabi
Multiscale Modeling of Biological Flow using Lattice Boltzmann Method

Defense Date

Dr. Yaling Liu

Dissertation Director

Approved Date

Committee Members

Dr. Alparslan Oztekin

Dr. Arindam Banerjee

Dr. Yue Yu

Acknowledgments

First and foremost, I would like to thank my advisor, Professor Yaling Liu, for his guidance and support during my PhD studies at Lehigh University. His mentoring in research, his patience and motivation helped me a lot during all my research projects and in writing the dissertation. He held me to a high standard whiles allowed for lots of freedom on the project selection to capitalize on my strength. Without his guidance and support, this dissertation would have not been possible. I am grateful to Prof. Banerjee, Prof. Oztekin, and Prof. Yu for being on my committee. Their guidance and expert advice when reading through my research were very helpful, and they also provided useful feedback and suggestions. I would like to express my gratitude to all faculty members for their scientific advice and the great courses offered in the Mechanical Engineering department. I am also grateful to Dr. Jifu Tan for the collaboration on Lattice Boltzmann code developing project. My gratitude is extended to all of my lab mates including but not limited to Doruk Yunus, Ran He, Christopher Uhl, Shunqiang Wang, Wentao Shi, Antony Thomas, Meghdad Razizadeh, Yihua Zhou, and Jia Hu. My gratitude is extended to all present and past Bio-Nanomechanics group members and friends for numerous interesting discussions on scientific matters. I should thank them for a friendly and collaborative environment in the group and I should say that it is joyful to work with you all. So far from home. I am in debt to my wife Sarah and want to express my deepest gratitude for her love, patience and

tremendous support and encouragement during the four years at Lehigh University. Last but certainly not least, I thank my parents and family for their unconditional support throughout all these years.

Contents

List of Tables

List of Figures

Abstract

In this dissertation, we have developed a fluid-structure interaction code specifically designed to simulate soft microparticle deformation in biological flow. We have used this tool for two different applications. First, we study red blood cell deformation under shear flow to evaluate stress distribution on membrane and subsequently pore formation on RBC membrane. Second, we utilized this code to show a proof of concept for an idea where we can separate soft particles based on their biophysical properties. In the following, these applications are discussed in more details.

Under high shear rates, pores form on RBC membrane through which hemoglobin leaks out and increases free hemoglobin content of plasma leading to hemolysis. We hypothesize that local flow dynamics such as flow rate and shear stress determines blood cell damage. In this dissertation, a novel model is presented to study red blood cell (RBC) hemolysis at cellular level. The goal of the proposed work is to establish multiscale computational techniques to predict the blood cell dynamics and damage in complex flow conditions, i.e., blood-wetting biomedical devices. The cell membrane damage model will be coupled with local fluid flow to study cell deformation and rupture and a generalized cellular level blood cell damage model will be developed based on these simulations. By coupling Lattice Boltzmann and spring connected network models through immersed boundary method, we estimate hemolysis of a single red blood cell under various shear rates. First, we use

adaptive meshing to find local strain distribution and critical sites on RBC membrane, then we apply underlying molecular dynamic simulations to evaluate damage. Our approach is comprised of three sub-models: defining criteria of pore formation, calculating pore size, and measuring Hb diffusive flux out of pores. Our damage model uses information of different scales to predict cellular level hemolysis. Results are compared with experimental studies and other models in literature. The developed cellular damage model can be used as a predictive tool for hydrodynamic and hematologic design optimization of blood-wetting medical devices.

Isolating cells of interest from a heterogeneous mixture has been of critical importance in biological studies and clinical applications. In this dissertation, we have proposed to use ciliary system in microfluidic devices to isolate target subpopulation of soft particles based on their biophysical properties. In this model, the bottom of microchannel is covered with an equally spaced cilia array which can be magnetically actuated. A series of simulations are performed to study cilia-particle interaction and isolation dynamic. It is shown that these elastic hair-like filaments can influence particle's trajectories differently depending on their biophysical properties. This modeling study also uses immersed boundary (IB) method coupled with lattice Boltzmann method. Soft particles are simulated by connected network of nonlinear springs. Moreover, cilia is modeled by point-particle scheme. It is demonstrated that active ciliary system is able to continuously and non-destructively sort cells based on their size, shape and stiffness. Ultimately, a design map for fabrication of a programmable microfluidic device capable of isolating various subpopulation of cells is developed. This biocompatible, label-free design can separate cells/soft microparticles with high throughput which can greatly complement existing separation technologies.

Chapter 1: Introduction

1.1 Introduction to computational fluid dynamics

With invention of calculus, scholars have started studying fluid mechanics using partial differential equations (PDE). The most widely used fluid model is incompressible Navier-Stokes (NS) equations which can be simply written as

$$\nabla . u = 0 \tag{1.1}$$

$$\frac{\partial \mathrm{u}}{\partial \mathrm{t}} + \mathrm{u}.\nabla u = -\nabla \mathrm{p} + \nu \nabla^2 \mathrm{u} + \mathrm{f} \tag{1.2}$$

where u is the velocity vector, ν is the kinetic viscosity, p is the pressure, t is the time, f is the body force. Eqn(1.1) represents the conservation of mass while Eqn(1.2) is basically Newton's second law of motion for fluid. It should be noted that typically there are four unknowns in NS equations, three components of velocity as well as pressure distribution. Generally, given sufficient initial and boundary conditions, there is no analytical solutions for this nonlinear second order partial differential equations.

For a lot of industrial application, we need to have a better understanding of flow field to recognize the source of phenomena. For instance, from intuition we may know that particles align under shear flow [1, 2]. However, to understand the relation between viscosity and alignment, we need to look at fluid dynamic of this phenomena. Computational fluid dynamics (CFD) is a field of study in fluid mechanics that employ numerical methods to solve fluid flows field. Our group in Lehigh University has done many bio-related CFD studies. We specifically are focused on studying drug delivery [3-7]. Generally, all CFD methods can categorized into continuum and particle based approaches. Continuum mechanics based algorithms use mesh to discretize the continuous domain described in the NS equation. In this way, the partial differential equations are replaced by a set of algebraic equations. The most widely used approach is finite volume method where the integral form of conservation equations are used. In contrary, the idea for particle based method is originated from molecular dynamics.

Atomistic methods such as the Molecular Dynamics (MD) and the Monte Carlo (MC) techniques provide a detailed system description on the level of a single atom where length and time scales are very small [8]. These simulated systems can only be used for very small sizes and times on the order of nanometers and nanoseconds because of its high computational expense. Mesoscopic approaches such as Lattice Boltzmann method (LBM)[5], Dissipative Particle Dynamics (DPD) [9] provide a "coarse-grained" description of a modeled system by keeping some molecular details which is necessary to capture some physics of the system. In this dissertation, we specifically focus on using the Lattice Boltzmann Method (LBM).

Particle based LB method is different from traditional NS solver where they explicitly solve pressure and velocity distribution. Instead, it uses particle distribution function which is the probability density of finding gas molecules in the phase space. All other macroscopic variables such as velocity and pressure are derived from the particle distribution function. LBM also has many advantages over conventional CFD methods. For instance, its algorithm can be easily parallelized where streaming and collision steps only use the nearest neighboring information. Moreover, it can be easily modified to model convective heat transfer and multiphase flows. In these cases, we can use different distribution functions and interaction models to model temperature distribution, phase separation and even phase transition. Furthermore, unlike conventional CFD method where Poisson equations is solved to derive pressure, in LBM pressure term is directly obtained from the equation of state.

Multiscale modeling is an interdisciplinary rapidly developing area with its applications in various fields such as engineering. Many realistic problems require accurate modeling across several orders of magnitude in spatiotemporal scales. Thus, these multiscale methods can be used to bridge between various spatiotemporal scales. These algorithms attempt to put together several existing approaches that cover different ranges of space and time scales. Several recently developed hybrid methods include MD-NS coupling [10], and MD-LBM[11]. The major contribution of this work to hybrid multiscale approaches is devoted to the development of a multiscale red blood cell (RBC) model which is then applied to blood flow modeling. In this dissertation, we specifically focused on developing a fluid-solid interaction code using LBM, spring network model and immersed boundary method. Using this tool, we were able to address questions regarding shear-induced red

blood cell damage and model sorting process using active ciliary system. In the following, we will first discuss the importance of studying red blood cell hemolysis.

1.2 Red blood cell Shear-Induced Hemolysis

Blood consists 7-8% of human body weight and is a concentrated suspension containing red blood cells (RBCs), white blood cells (WBCs), blood plasma, platelets, sugar, fat, protein, and salt solution.

Blood related disorders such as sickle cell hemoglobin disease, coronary heart disease, blood coagulation, may critically change normal blood circulation throughout the body [12]. The blood volume fraction of RBCs is approximately 45%, of WBCs below 1%, while the rest of the volume is almost plasma. Thus, RBCs is directly responsible for the non-Newtonian characteristics of blood. RBCs are highly deformable and has biconcave discoid shape with a diameter of approximately 8 μm and a thickness of 2 μm. This unique mechanical characteristic of red blood cells allows them to pass through very narrow capillaries with a diameter as small as 3 μm.

In blood-wetting devices such as hemodialysis machine, artificial heart [13], prosthetic heart valve[14], ventricular assist devices (VADs) and bio-printers [15], blood cells are under various flow induced stresses. In these medical devices, mechanical stresses can be up to two orders of magnitude higher than its physiologically relevant range [16, 17]. Prolonged contact and collision between blood cells and device surfaces and regions of high shear stress leads to cell damage [18, 19]. Figure 1.1 shows some examples of biomedical devices and processes where cells may be damaged. In these examples, cells

are subjected to combined effects of shear, tension and compression. When cell is damaged, hemoglobin (Hb) is released into plasma which in severe cases may lead to renal failure, anemia, arrhythmias, and death [20-22]. In milder cases, Hb is released through temporary pores on the Red blood cell (RBC) membranes which may lead to other pathologies. Red blood cells (RBCs) damage induced by ventricular assist devices (VADs) over a long period of time is still one of the issues to be addressed [23]. Moreover, acute hemolysis is an unavoidable side effect of extracorporeal circulation in regular 4-hour, three times per week dialysis [24].

Erythrocyte membrane can also be damaged by osmotic swelling [25], transient electrical field [26], temperature jump [27]. Mechanical hemolysis caused by filtration through micropores with mean pore diameters of 2.2–4.4 μm showed that intracellular content release increase with smaller pore size and higher pressure gradient [28]. Individual RBC damage was reported as irreversible deformation and fragmentation when placed in concentric cylinder viscometer under pure shear flow[29]. Fragmentation can first be detected in 2,500 dyne/cm2 shear rate[29]. Nanoscale pores on the membrane of mechanically traumatized erythrocytes was recently visualized using atomic force microscope (AFM) and reported as the initial stages of damage [30]. Damage evaluation at the cellular level is particularly important for regions where flow shear stress is changing dramatically across cell dimensions, e.g., when cells are physical contact with medical device surfaces with complex structures such as stents [31, 32] and blood pump blades [13]. Subject to mechanical stress, the cell membrane first becomes thinner and then pore formation begins. RBC membranes can support an approximated areal strain of 6% before

rupture [33]. If the applied stress is sustained, the pore will enlarge until the membrane is ruptured, leading to cell apoptosis and cell necrosis and loss of viability [34-36].

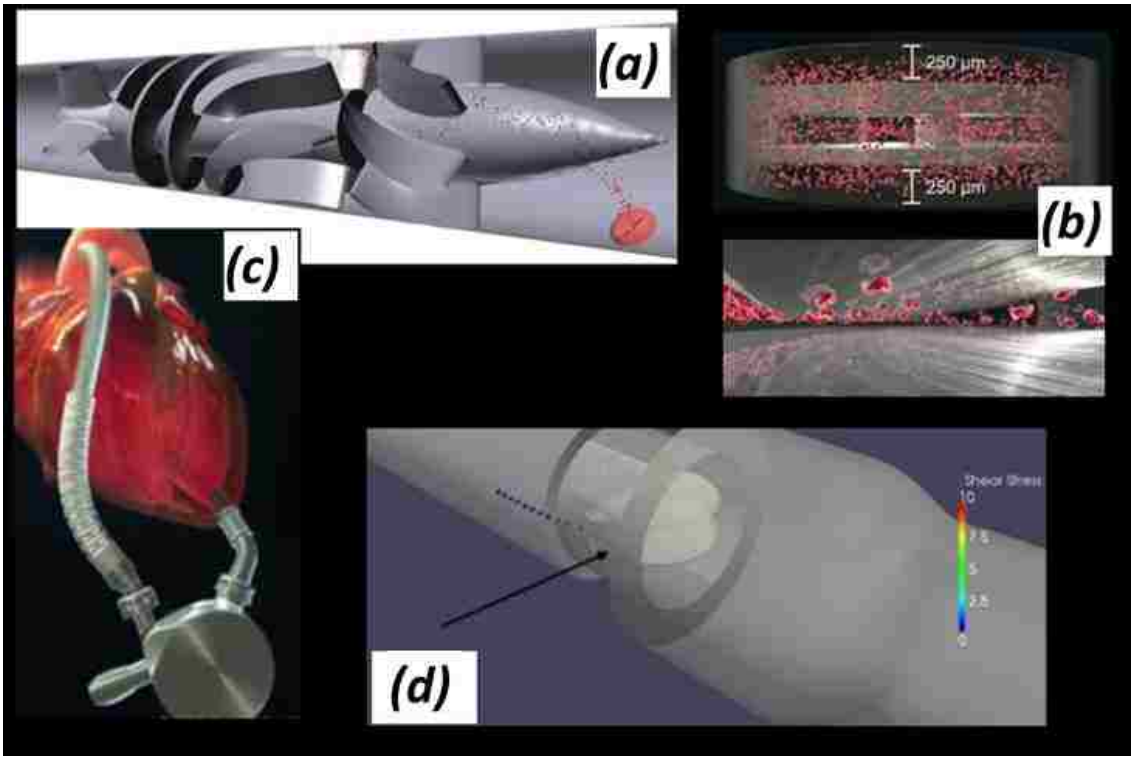

Figure 1.1. Examples of biomedical devices and processes where cell may be damaged. (a) A continuous flow, centrifugal blood pump[37]; (b) ventricular assist device with blood sheared between rotating disks, (c) Micromed DeBakey axial blood pump[38]; and (d) Bilieaflet mechanical heart valve[39].

A maximum shear stress of 250 Pa is widely used as the design criterion in the development of VADs [40]. The consequence of RBC damage can be sudden, and potentially fatal. The damage induced nitric oxide depletion results in pulmonary hypertension, abdominal pain, and some other physiological dysfunctions[41]. Thus, it is very important to evaluate the blood damage for safety evaluation of blood-wetted medical devices. The blood cell damage in these blood-wetting devices are mainly induced by local stresses applied on the cell membrane. In order to evaluate blood cell damage, the molecular level information of

pore formation on the membrane needs to be linked with the cellular scale cell deformation and macroscopic flow condition.

Computer simulation and experimental assessment are crucial tools for blood damage evaluation. Since 2012, the Federal Food and Drug Administration (FDA) have made tremendous efforts to benchmark and establish standards to evaluate blood damage in medical devices [42-45]. Flow patterns within medical devices have significant influences on blood damage. The FDA would like to relate important flow parameters such as shear stress, cell exposure times to adverse biologic responses such as hemolysis, and platelet activation. A simple nozzle and a more complex blood pump model of specific geometries were proposed for the standardization of blood damage safety. Multiple volunteer groups signed up and performed computational fluid dynamics (CFD) simulations to predict blood damage in these models under the same given flow condition. The damage of red blood cells is difficult to be directly visualized due to the small size of the blood cells (5-10μm) and the fast flow speed.

In experimental setup, the extent of hemolysis is typically assessed through the amount of plasma-free hemoglobin (pfHb) measured by flowing blood in microcirculation loops of the perfused artificial device. For instance, Giersiepen et al. [46] estimated shear-related blood damage in 25 heart valve prostheses. Zhang et al. [47] used a novel couette-type blood-shearing devices to study Hemolysis. Complementing experimental works, the damage criteria in CFD works relied on an empirical formula from experiments that correlates shear stress and exposure time to the free hemoglobin in blood plasma released from damaged RBCs. Specifically, fitting experiment data, empirical correlations were proposed to estimate hemolysis as a function of shear stress and exposure time. Due to the

complex geometries and flow conditions of various devices, as well as the macroscopic nature of free hemoglobin measurement, parameters obtained from these tests are only applicable to that specific device. Also, they cannot provide sufficient insight into flow-induced damage at cellular scale.

Bludszuweit [48], Yeleswarapu et al. [49] and Okamoto et al. [50] developed a hemolysis model for VADs where hemoglobin release is correlated with shear rates and the exposure time that cells are subjected to. The stress history of RBCs along their streaklines was obtained by Lagrangian particle tracking. With integrative computation, cumulative RBCs damage were measured. Instead of using a simple shear stress scalar, Dhruv et al [51, 52] incorporated a more complicated formulation for shear using a tensorial strain model to predict hemolysis based on RBC deformation. These CFD-based models rely on macroscale experimental estimation of damage in specific devices and lack a general blood cell damage evaluation criterion, where cellular level information is required.

Empirical correlations are widely used for estimation of flow-induced hemolysis in blood-contacting medical devices. Most of them use power law to correlate shear stress, exposure time and index of hemolysis ($IH = A\tau^{\alpha}t^{\beta}$). In Giersiepen et al.'s study [46], A, α and β are estimated as 3.62×10^{-5}, 2.416 and 0.785, respectively whereas in the recent study of Zhang et al. [47], $A = 1.228 \times 10^{-5}, \alpha = 1.9918$ and $\beta = 0.6606$ are suggested. Zhang et al.'s formula [47] predicts 0.1% hemolysis for exposure time of 887ms under a shear rate of $30{,}000s^{-1}$ while Giersiepen et al. 's formula [46] estimates 1% hemolysis under the same flow condition. One order of magnitude difference between these

experimental works suggests that empirical estimations strongly depends on test device and experimental condition.

There are also continuum cellular damage models based on the strain energy density [53-55]. However, those models do not consider the physics of pore formations and hemoglobin release. A more comprehensive multiscale model of sublytic damage is proposed by Vitale et al. [56] where they assume the nucleation of pores is dictated by the membrane energy landscape of the perturbation. Assuming pores relieve the tension and minimize the total free energy, they derived analytical expression for pore radius and density under shear rates ranging from $4{,}000s^{-1}$to $42{,}000s^{-1}$. Their descriptions of pore radius and density are a function of membrane areal strain varying from 0.16% to 6%. Other researchers have performed Molecular Dynamics (MD) simulations [8] of pore structure in the bilayers [57] as well as membrane disruption and rupture using dissipative particle dynamics [58] and Monte Carlo simulation [59]. Cytoskeletal dynamics of human erythrocyte is specifically studied by Li et al. [60] where they used Coarse-grained simulation to elucidate the roles of shear stress, specific chemical agents, and thermal fluctuations in cytoskeleton remodeling. To the best of our knowledge, yet there is no existing model which linked cellular level damage to hemoglobin release. Table. 1 summarizes some literature works on RBC damage evaluation.

Table 1.1. Summary of some cell damage researches reported in literatures.

Ref.	Approach/ Tool	Findings/ Target device	Year
Giersiepen [46]	Experimental estimation	In vitro comparison of 25 prosthetic heart valve $\frac{\Delta Hb}{Hb} = 3.62 \times 10^{-7} \sigma^{2.416} \Delta t^{0.785}$	*1990*
Yeleswarapu [49]	Mathematical Stress-based model	Included loading history and Damage accumulation in rotatory blood pump	*1995*
Arora [51, 52]	strain-based hemolysis model - Ellipsoidal droplet - CFD	$\frac{\Delta Hb}{Hb} = 3.62 \times 10^{-7} \left(\mu_{\text{blood}} \sqrt{\frac{f_1^2 D^2}{(1-D^2) f_2^2}} \right)^{2.416} t^{0.785}$ - VADs	*2004*
Yangsheng [54]	Experiments τ = 5000 dyn/cm^2- Digital camera–ellipsoidal assumption	Captured images of deformed cells. Calibrated simple mathematical model - Simple channel	*2010*
Zhang et al. [46]	Experimental estimation	Novel Couette-Type Blood-Shearing Devices $IH_{\text{flow}} = 1.228 \times 10^{-5} \times \tau^{1.9918} \times t^{0.6606}$	*2011*
Vitale [61]	Multiscale strain based model	Included hemoglobin transport dynamic	*2014*
Ezzeldin [55]	3D Strain-Based/Coarse-grained RBC Model	Included complex shape distortions of RBCs and damage in prosthetic heart valves	*2015*

Cell damage occurs at different scales from nanoscale membrane pore initialization to microscale cell membrane rupture. In this dissertation, we developed a multiscale model to evaluate blood cell damage under shear flow conditions. Development of a multi-scale model which can directly correlate the microscale state of the cell membrane to local stresses is needed. Such a multiscale model could serve as a predictive tool for hematologic biomedical device design and optimization. In order to evaluate blood cell damage, the molecular level information of pore formation on the membrane needs to be linked with the cellular scale cell deformation and macroscopic flow condition. The goal of this dissertation is to establish computational techniques to predict the blood cell dynamics and

cellular damage under complex flow conditions. Spring connected model [5, 62, 63] of erythrocyte membrane is coupled with lattice Boltzmann [5] through immersed boundary (IB) method [64-68] in order to calculate local strain/stress of RBC membrane and study hemolysis as Hb molecules leaks out of the damaged regions. Our damage model is comprised of three sub-models where we identify criteria for nanopores formation, determine pore dimensions, and finally calculate Hb diffusion out of porated regions as shown in Figure 1.2. Unlike previous continuum approaches, we study cellular hemolysis by obtaining model parameters from underlying molecular dynamic simulations.

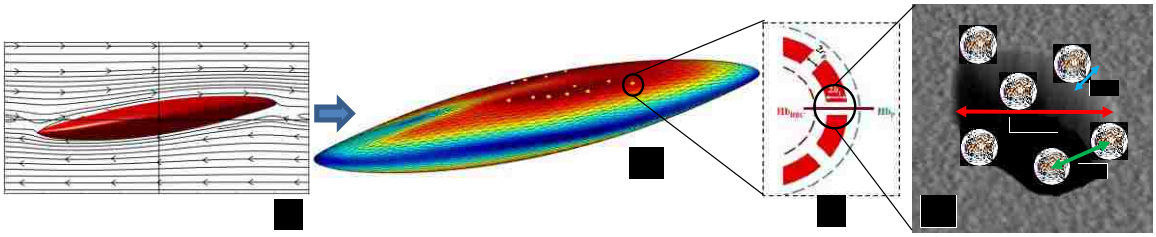

Figure 1.2. The summary of multiscale cell damage model; (a) RBC deformation under shear flow; (b) Local strain distribution and nanopore formation; (c) Hb diffusion out of porated regions; (d) Schematic of Hb molecules diffuse out of membrane pore.

1.3 Label-free Sorting of Soft Microparticles

In United States, cancer is currently the leading cause of death for young generation and has surpassed heart disease [69]. Metastasis is basically the spread of a cancer from the primary tumor site to the other parts of the body. Metastasis is responsible for about 90% of the cancer deaths [70]. The chance of full recovery can be significantly enhanced if the cancer is diagnosed in early stages. Thus, detecting circulating cancer cells (CTCs) is very critical. However, it is very challenging because CTCs are rare event. There are only a few CTCs mixed with millions of WBCs and a billion of RBCs in 1 mL blood sample. Many

different methods have been employed to enrich CTCs such as using electric field[71], magnetic field [72], and optical force[73]. Alternatively, specific binding between receptors on cancer cell membrane and ligands coated on the surface of microfluidic channel have been used to capture CTCs [74]. These approaches may require sophisticated cell preparation, careful microfluidics design, or external fields to capture CTCs. On the other hand, there are methods which use cell physical properties such as deformability to separate CTCs [75]. In the following, we will discuss current methods for isolating target cells from heterogonous mixture.

Separating particles from a mixture has been recently attracted may attention in biological studies and clinical applications such as rare cell isolation, capturing circulating cancer cells and single cell sequencing [75-77]. Different physical mechanisms such as electric fields[78, 79], magnetic fields[80, 81], acoustic fields[82, 83] and optical forces[73, 84] have been recently used to manipulate cells. Recently, acoustic forces have been used for separation, alignment, and enrichment of particles or cells[85, 86]. Specifically, standing surface acoustic waves are being explored for continuous separation of particles based on their volume, density and compressibility[83, 87]. Alternatively, cells can also be labelled through specific binding of fluorescent antibodies in order to separate cells using devices such as fluorescence activated cell sorters (FACS)[88]. This specific isolation method is expensive and may damage cells during the sorting process. Other mechanisms such as valve-based switching[89] and hydrodynamic flows[90] can also be used to isolate a target subpopulations of cells. Asymmetric bifurcations in laminar flow[91] and hydrodynamic filtration[92] are also another way to do size-dependent separation of particles continuously. Generally, low biocompatibility, bulky instrument, and low throughput can

be mentioned as drawbacks of discussed separation methods. Thus, a biocompatible label-free method that can separate cells with high throughput will be very useful and will significantly complement existing isolation technologies.

It has been widely shown that with increasing metastatic efficiency in human cancer cell lines, stiffness of cells are reduced [93]. Therefore, we can utilize mechanical stiffness to detect target cell populations in early diagnosis of cancer and infectious diseases [75]. Lab on chip microfluidic devices are a great addition to this type of studies where we can enrich cell populations based on mechanical stiffness[94, 95]. One of the limitation of current methods is that it is very challenging to isolate rare cells from a mixture based on slight difference in their mechanical stiffness compared to regular cells. However, it is reported that it is relatively easier to sort particles based on their shape and size. In this dissertation, we aim to propose a novel approach by harnessing the specific characteristics of active ciliary systems for isolating particles based on shape, size, and stiffness. Based on previous cilia-microparticle interactions studies, the hydrodynamic forces induced by beating cilia can regulate the trajectories of the suspended particles based on their biophysical properties. To best of our knowledge, the possibility of using active ciliary system to separate particles has not been previously studied.

1.4 Bioinspired Synthetic Cilia Array

Various biological organisms use the coordinated motion of ciliary system to capture food [96] or even prevent settlement of fouling agents [97]. Furthermore, cilia covering the upper generations of human lung airway is very important for removing unwanted

particulates out of the respiratory tract[98]. On the other hand, artificial cilia are being utilized to control fluid flow in microfluidic devices in order to enhance its performance. Moreover, these synthetic cilia is widely used in lab-on-chip devices for other purposes such as pumping and mixing [99] or to prevent fouling of microfluidic devices[100]. These ciliary systems are generally long, flexible pillars anchored to the walls of microchannel. It should be mentioned that for active ones, they can be actuated by external electromagnetic fields[99].

In literature, several methods has been proposed to fabricate synthetic cilia in micro-scale and there are different mechanism to actuate them. For example, by applying a voltage difference between two layers of double layer polyimide (PI) and chromium (Cr) microbeam, we can electrostatically actuated[101] them. It can operate at $200 Hz$ and generate a local mean fluid velocity of $500 \mu m/s$[101].

Furthermore, magnetic-actuated cilia made from polydimethylsiloxane (PDMS) contain superparamagnetic nanoparticles (Fe_3O_4) which can create a net fluid flow of about $8 \mu m/s$ at frequencies up to $35 Hz$[102]. They can be fabricated by using polycarbonate track etch (PCTE) filter membrane as mold which later in the process can be dissolved. There are also resonance-actuated[103]and hydrogel-actuated[104] synthetic cilia which are fabricated with soft lithography method. In the first one, cilia oscillates in resonance with piezoelectric while in the second one the change in pH lead to shrinkage or swelling of the hydrogel.

In literature, there are serval theoretical and computational studies on cilia−microparticle interactions [105-108]. It is reported [106, 109] that depending on the frequency of beating

cilia, the microparticles can be either driven downward toward the substrate or repelled away from ciliary assay[105]. For example, the hydrodynamic forces generated by active motion of ciliary systems significantly can help capturing microparticles within the grafted pillars[110]. It is also shown that even passive motions of artificial cilia can improve deposition [111] or avoid adhesion of sticky particles[112]. To summarize, final state of particle with respect to ciliary system can be released, propelled or propelled [113]. It is worthy to mention that these previous studies are using cilia with sticky tips. Such adhesive tip is responsible for downward force toward ciliated region.

In this dissertation, we did a modelling study to study hydrodynamic interactions of active ciliary assay with soft particulates in more detail. In our model, the bottom wall of microfluidic channel is covered with an equally spaced cilia array. To include cells and cilia, spring connected network model is coupled with lattice Boltzmann through immersed boundary (IB) method. It is shown that in 3D channel, particles with different physical properties move at different heights above cilia array. Our novel method is able to continuously and non-destructively sort soft microparticles into subpopulations with high throughput. In the following chapter, the formulations and complete description of our fluid-cell interaction model that is used for both discussed projects is explained in detail.

Chapter 2: Lattice Boltzmann method

Lattice Boltzmann Method is originated from Lattice Gas Automata over two decades ago. From then, it has been widely used as an alternative tool to solve fluid dynamics. It is noteworthy to mention that LBM is capable of modeling multiphase flow [114], convective heat transfer[115], and phase transition in high-density ratio flow systems[116]. One prominent advantage of LBM is that simple algorithm structure in local streaming and collision steps makes it considerably easy to take advantage of parallel computing. In the following, LBM and its relevant formulations are discussed in more detail.

2.1 Lattice BGK Model

Attracted by its particulate nature and parallel computing capabilities, the Lattice-Boltzman Method (LBM) has been developed and is used as the fluid solver in current study [5]. Algorithms of LBM are reported extensively in literature [117-119]. LBM is typically

considered as a second order accurate method in space and time[120]. The key concept in standard lattice Boltzmann is the particle distribution function$f_i(x,t)$ at phase space $(x,\overrightarrow{c_i})$ at time t, where $\overrightarrow{c_i}$ is the discretized velocity. The LBM dynamics involve streaming and collision step. It should be noted that Bhatnagar-Gross-Krook (BGK) collision scheme [121] is used in this dissertation.

$$f_i(x+\Delta t\overrightarrow{c_i},t+\ \Delta t)-\ f_i(x,t)=-\frac{\Delta t}{\tau_f}\left[f_i(x,t)-f_i^{eq}(x,t)\right]+F_i \qquad (2.1)$$

where τ_f is the PDF relaxation time, $f_i^{eq}(x,t)$ is population distribution at equilibrium, Δt is time step in lattice unit, and i is the index of discrete particle velocities. The terms on the left hand of the equation represent streaming step while the right hand side F_i is the force term and first term is collision operator. Note that the force term is important where the existence of cell domain is replaced through a force density or to create a separation force between phases in multiphase flow systems. The details are discussed in the cell-fluid coupling section. The corresponding equilibrium distribution function, $f_i^{eq}(x,t)$, is related to the local macroscale fluid velocity u and can be defined as

$$f_i^{eq}=\omega_i\rho\left[1+\frac{e_i.u}{c_s^2}+\frac{(e_i.u)^2}{2c_s^4}-\frac{u^2}{2c_s^2}\right] \qquad (2.2)$$

where ω_i is the weight coefficients and c_s is speed of sound in LB scheme. In low Reynolds number flows, such as the flow in microfluidic devices, we can simulate stokes flow by simplifying the equilibrium distribution function as

$$f_i^{eq}=\omega_i\rho\left[1+\frac{e_i.u}{c_s^2}\right] \qquad (2.3)$$

Macroscale density and velocity can be obtained as

$$\rho(x,t) = \sum_i f_i(x,t) \tag{2.4}$$

$$\rho(x,t)\,\vec{u}(x,t) = \sum f_i(x,t)\overrightarrow{c_i} \tag{2.5}$$

Several different lattice structures can be utilized to solve fluid flow such as D2Q6, D2Q7, D2Q9, D3Q13, D3Q15, D3Q19, D3Q27, etc. For instance, D2Q9 represents a 2D lattice structure with 9 discretized velocity vectors. The criteria to determine the efficient lattice structure is to achieve the highest order of accuracy with minimum number of discrete velocities. The most widely used lattice structures are D2Q9 for 2D and D3Q19 for 3D simulations as shown in Figure 2.1.

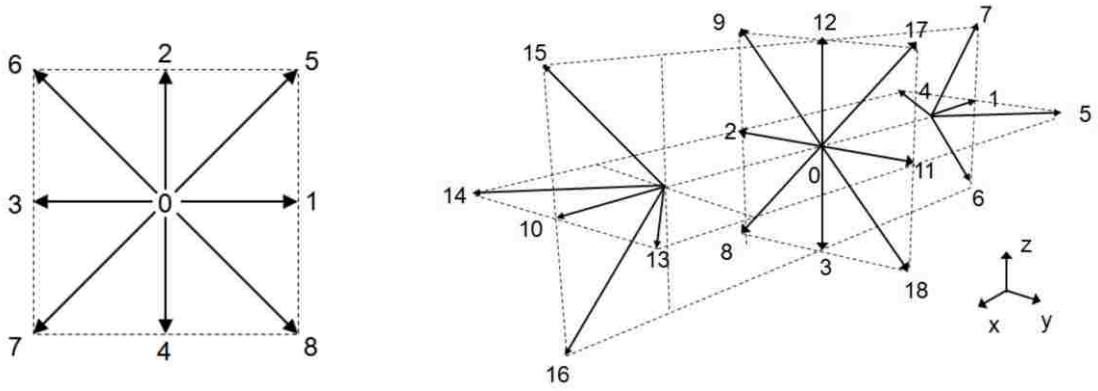

Figure 2.1. Illustration of (a) D2Q9 and (b) D3Q19 lattices.

The weighting factor and discrete velocity for D2Q9 lattice structure are given as

$$e_i = \begin{cases} (0,0,0) & \alpha = 0; \\ (\pm 1,0)c, (0,\pm 1)c, & \alpha = 1,2,\dots,4; \\ (\pm 1,\pm 1)c, & \alpha = 5,6,\dots,8; \end{cases} \tag{2.6}$$

$$\omega_i = \begin{cases} 4/9 & \alpha = 0; \\ 1/9 & \alpha = 1,2,\dots,4; \\ 1/36 & \alpha = 5,6,\dots,8; \end{cases} \quad (2.7)$$

Furthermore, the weighting factor and discrete velocity for D3Q19 lattice models can be written as

$$e_i = \begin{cases} (0,0,0) & \alpha = 0; \\ (\pm 1,0,0)c, (0,\pm 1,0)c, (0,0,\pm 1)c, & \alpha = 1,2,\dots,6; \\ (\pm 1,\pm 1,0)c, (\pm 1,0,\pm 1)c, (0,\pm 1,\pm 1)c, & \alpha = 7,8,\dots,18; \end{cases} \quad (2.8)$$

$$\omega_i = \begin{cases} 1/3 & \alpha = 0; \\ 1/18 & \alpha = 1,2,\dots,6; \\ 1/36 & \alpha = 7,8,\dots,18; \end{cases} \quad (2.9)$$

The total force acting on a fluid particle in flow may origin from different sources, such as gravity or force exerted by structure deformation

$$F_T = F_g + F_{cell} \quad (2.10)$$

where F_{cell} is the cell–fluid interaction force, and F_g represents gravitational force. The existence of external bodies in the flow are introduced through a force term, F_i, expressed in terms of external body force density $\vec{f}$ and fluid macroscale velocity $\vec{u}$.

$$F_i = \left(1 - \frac{1}{2\tau}\right) w_i \left(\frac{\vec{c_i} - \vec{u}}{c_s^2} + \frac{\vec{c_i}.\vec{u}}{c_s^4}\vec{c_i}\right).\vec{f} \quad (2.11)$$

It should be noted that $\vec{f}$ is derived from solid model which is distributed on lattice nodes via Immersed Boundary method. There are also other formulations to incorporate force term such as velocity shifting method and discrete force method [122]. More detail information concerning these approaches can be found in [122] where it is shown that EDM has better accuracy and stability.

2.2 Unit conversion

It is not convenient to solve Lattice Boltzmann Equations in physical units. In what follows, the conversion between physical units and lattice units will be discussed. It should be noted that the kinematic viscosity in lattice unit is related to the single relaxation τ which are given by

$$\upsilon_{LB} = c_s^2 \left(\tau_f - \frac{1}{2}\right) \Delta t_{LB} \tag{2.12}$$

where τ_f are relaxation, c_s is speed of sound and Δt_{LB} is time step in lattice unit. To convert parameter, characteristic time, length and mass in both physical and lattice units should be calculated first. And then Reynolds dimensionless number connect physical parameters to lattice units and can be defined as

$$Re = \frac{U_{Phy} L_{char}}{\upsilon_{Phy}} = \frac{U_{LB} L_{LB}}{\upsilon_{LB}} \tag{2.13}$$

Using characteristic scales, we can identify characteristic velocity in both units by following equations.

$$U_{phy} = \frac{L_{phy}}{t_{phy}} = \frac{N_{mesh} \times \Delta x_{char}}{N_{iter} \times \Delta t_{char}}$$
$$U_{LB} = \frac{L_{LB}}{t_{LB}} = \frac{N_{mesh} \times \Delta x_{LB}}{N_{iter} \times \Delta t_{LB}} \quad (2.14)$$

where N_{mesh} is the number of mesh in characteristic length scale; N_{iter} is the number of iteration during characteristic time scale. Typically, it is very convenient to assume $\Delta t_{LB} = 1$, $\Delta x_{LB} = 1$, and $c_s = 1/\sqrt{3}$ in lattice units. Using discussed relations, physical time step can be derived as

$$\Delta t_{phy} = \frac{L_{phy}^2}{N_{mesh}^2} \times \frac{(\tau_f - 0.5)/3}{\upsilon_{Ref}} \quad (2.15)$$

In practice, typically τ_f and N_{mesh} are two parameters that are free to tune by the user for athermal flows. Thus, by tuning N_{mesh}, and τ_f and inputting υ_{Ref} and L_{phy}, the time step in physical system can be simply calculated. The acceptable range for relaxation time is between 0.5 and 2.The closer it get to 0.5, more unstable LB simulation will be. Generally, depending on Reynolds numbers the recommended range of τ_f is between 0.8 and 1. τ_f close to 0.5 or greater than 1 will result in inaccuracies in the simulation. Furthermore, Mach number in lattice unit can be rewritten as

$$Mach = \frac{U_{LB}}{c_s} = \sqrt{3} \times \frac{N_{mesh}}{N_{iter}} \quad (2.16)$$

Lattice Boltzmann method is typically considered as a second order accurate scheme in both space and time for the simulation of weakly compressible, athermal flows at small Mach numbers. Obviously, the Mach number in lattice unit cannot be larger than one, since it is basic intuition that the distribution function information should be able to transfer

faster than fluid flow. Thus, N_{iter} should be much larger than N_{mesh} and this criteria should be considered during unit conversion as well.

Additionally, in simulations involving deformable capsules in biological flows, the viscosity difference across the membrane is important. In human RBCs, the interior cytoplasm is five times as viscous as the surrounding plasma. This viscosity difference influence the RBC dynamics and can be simply implemented by using different relaxation parameters inside and outside of the RBC.

2.3 Non-slip boundary conditions

Nonslip boundary conditions refer to the boundaries where the fluid velocity is zero. In LBM, bounce back algorithm is commonly utilized to implement stationary wall boundary condition. In half way bounce back, we just need to reflect all the populations on the lattice site in streaming step as shown in Figure 2.2. By this simple implementation of algorithm, we can see that there is no tangent or normal flux to the boundary surface. It should be mentioned that half way bounce back is second order accurate.

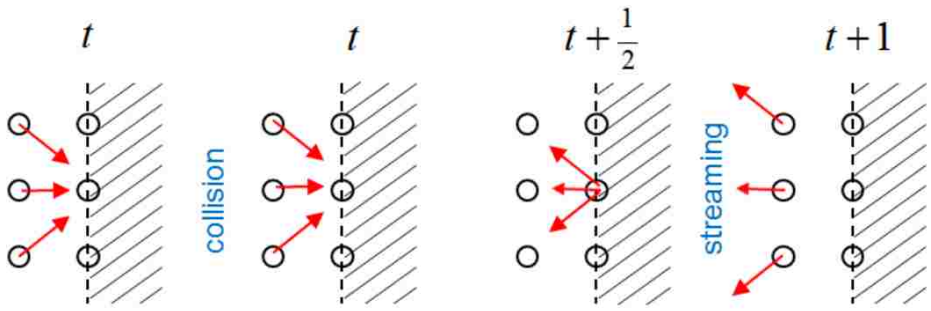

Figure 2.2. Schematic demonstration of half-way bounce back algorithm.

2.4 Velocity and pressure boundaries

To apply velocity or pressure boundary condition in LBM, we can use bounce back formulation on non-equilibrium part of the distribution function. Considering D2Q9 lattice structure, f2, f5, andf6 will be the unknown incoming distributions entering the domain as shown in Figure 2.3. For these unknowns, we can write the following equation

$$f_2 + f_5 + f_6 = \rho - (f_0 + f_1 + f_3 + f_4 + f_7 + f_8) \tag{2.17}$$
$$f_5 - f_6 = \rho u_x - (f_1 - f_3 + f_4 + f_8 - f_7)$$
$$f_2 + f_5 + f_6 = \rho u_y + (f_4 + f_7 + f_8)$$

Removing unknowns, we can calculate density at boundary nodes as

$$\rho = \frac{1}{1 - u_y}[f_0 + f_1 + f_3 + 2(f_4 + f_7 + f_8)] \tag{2.18}$$

And unknown distribution functions can be found using following equations

$$f_2 = f_4 + \frac{2}{3}(\rho u_y) \tag{2.19}$$
$$f_5 = f_7 - \frac{1}{2}(f_1 - f_3) + \frac{1}{2}\rho u_x + \frac{1}{6}\rho u_y$$
$$f_6 = f_8 + \frac{1}{2}(f_1 - f_3) - \frac{1}{2}\rho u_x + \frac{1}{6}\rho u_y$$

The same concept can be applied to D3Q19 as well. The detailed derivation and calculation formula for the incoming population distribution can be found in Ref.[123]. In LBM, applying pressure boundary condition is basically to specify the density at the boundaries. Generally the fluid density in LBM is initialized as unity over the whole fluid domain. Therefore, we need to first convert pressure difference into LB units, and then convert

pressure difference into density difference using equation of state. For the next step, we should add the density difference to the boundary that has higher pressure. Ultimately, by calculating the velocity component normal to boundaries using known distribution function, we can use Eqn(2.19) to update distribution functions for the next iteration.

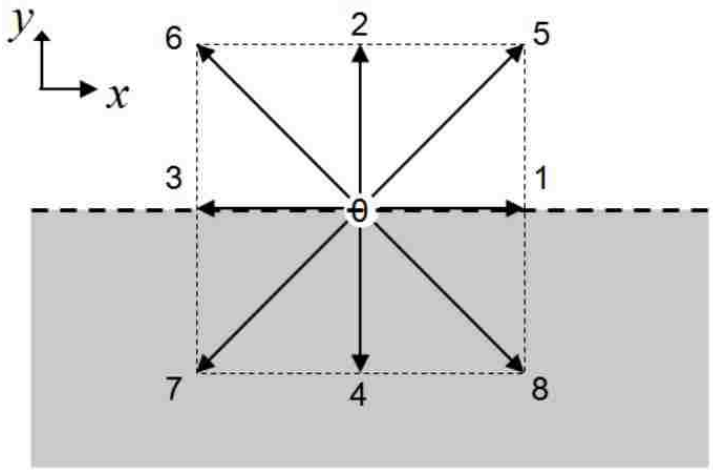

Figure 2.3. A lattice node on the bottom boundary surface. The shaded area is the boundary wall.

To incorporate cell in particulate flow [64, 67], SN model is also coupled with LBM through immersed boundary method. In what follows, SN methods and its relevant formulations are discussed.

2.5 Cell membrane model

In human circulation system, red blood cells (erythrocytes) occupy about 40% ~ 45% of the blood volume and don't have nucleus. They pick up oxygen (O_2) from the lung and deliver it to different organs throughout the body. RBCs have a biconcave shape with a diameter of 6-8μm and a thickness of 2 μm. The biconcave shaped and anucleate structure

enable RBCs to be squeezed through capillaries as small as 2 μm in diameter. At molecular level, the erythrocyte membrane mainly consists of a phospholipid bilayer and a spectrin network. The spectrin network forms a 2D hexagonal arrangement consisting of spectrin tetramers tethered to the membrane at junctional complex (actin) as well as ankyrins and band 3 protein. Each spectrin tetramer comprises two heterodimers that consist of intertwined and antiparallel α-spectrin and β-spectrin filaments. The mechanical properties of erythrocyte membrane is significantly influenced by spectrin network due to its large shear stiffness [124]. On the other hand, lipid bilayer resists bending and has a large local area stiffness but cannot sustain in-plane shear stress because the lipids and most of the proteins can diffuse freely within the membrane to relax the shear stress [125].

Basically, a spring connected network (SN) is a particle based cell model and is used to model erythrocyte membrane due to its simplicity in mathematical description [126-128]. The model is composed of nodes that are connected by springs [62] with nonlinear energy potentials. Specifically, the cell membrane consists of a set of vertex point $X_i, i \in \{1 \dots N_V\}$ that form a two-dimensional triangulated network. The vertices are connected by edges forming triangles. Thus, a membrane mesh is needed in coarse grained approach. The mesh is used to define the nodal position and membrane triangulation. RBC membrane mesh can simply be generated by subdividing an icosahedron several times into a target spherical mesh. Then we can map the spherical nodes into a biconcave shape following the formula suggested by [103].

$$Z(\varsigma) = \pm\sqrt{1-\frac{\varsigma}{r}}\left[\alpha_0 + \alpha_1\left(\frac{\varsigma}{r}\right)^2 + \alpha_2\left(\frac{\varsigma}{r}\right)^4\right] \tag{2.20}$$

where $\alpha_0 = 0.81\mu m$, $\alpha_1 = 7.83\mu m$, $\alpha_2 = -4.39\mu m$, and $\varsigma = \sqrt{x^2 + y^2}$ where x, y are the components in the spherical nodes (x, y, z). The potential energy of the system is defined as

$$V(\{x_i\}) = V_{in-plane} + V_{bending} + V_{area} + V_{volume} \tag{2.30}$$

The in-plane energy term characterizes the elastic energy stored in the membrane which include attractive nonlinear wormlike chain (WLC) and repulsive power function (POW) potentials. They are defined as

$$V_{in-plane} = \sum_{d\epsilon\ 1\ldots N_s} U_{WLC}(l_d) + U_{POW}(l_d) \tag{2.31}$$

$$U_{WLC} = \frac{k_B T l_m}{4p} \frac{3x^2 - 2x^3}{1 - x} \tag{2.32}$$

$$U_{POW}(l) = \begin{cases} \dfrac{k_p}{(m-1)l^{m-1}} & m > 1, m \neq 0 \\ -k_p \log(l) & m = 1, \end{cases} \tag{2.33}$$

where $x = l/l_m$, l_m is the maximum spring extension, p is the persistence length, $k_B T$ is the energy per unit mass, k_p is the POW force coefficient, and $m = 2$ is the exponent. Bending potential corresponds to bending stiffness of erythrocyte. The bending force is much more complicated than the forces in nonlinear springs. For the ease of discussion, Figure 2.4 shows two adjacent surfaces shared an edge where the bending energy is defined. The bending potential can be expressed as

$$V_{bending} = \sum_{d\epsilon\ 1\ldots N_s} k_b[1 - \cos(\theta_d - \theta_0)] \tag{2.34}$$

where k_b is the bending constant, θ_j is the instantaneous angle between two adjacent triangles having the common edge j, and θ_0 is the spontaneous angle. Third term in Eqn(2.30) stands for local and global area stiffness of lipid bilayer which is defined as

$$V_{area} = \frac{k_a(A - A_0^{tot})^2}{2A_0^{tot}} + \sum_{j\epsilon\ 1\ldots N_t} \frac{k_d(A_j - A_0)^2}{2A_0^{tot}} \tag{2.35}$$

where k_a and k_d are the global and local area constraint constants, respectively. Similarly, the last potential term conserves RBC volume

$$V_{area} = \frac{k_v(V - V_0^{tot})^2}{2V_0^{tot}} \tag{2.36}$$

where k_v is volume constraint constant. Finally, the nodal forces corresponding to the each energy can be calculated as $f_i = -\partial \mathrm{V}\{x_i\}/\partial x_i$. To calculate stress distribution on erythrocyte membrane, the springs and the hydrostatic elastic forces on triangulated network can be used to calculate stress components [129]. The stress is computed for mesh nodes surrounded by six triangular elements and are junction site of three pair-wise spring forces. Stress components can be calculated as

$$\tau_{\alpha\beta} = \tau_{\alpha\beta}^{WLC-POW} + \sigma_{\alpha\beta}^{area} = -\frac{3}{2\sum_{j=1:6} A_j}\left[\frac{f_{WLC-POW}(a)}{a} a_\alpha a_\beta + \frac{f_{WLC-POW}(b)}{b} b_\alpha b_\beta + \frac{f_{WLC-POW}(c)}{c} c_\alpha c_\beta\right] + \sum_{j=1:6} k_a \frac{(A_j - A_0)}{A_0} \delta_{\alpha\beta} \tag{2.37}$$

where $f_{WLC-POW}$ is summation of WLC and POW spring forces and equals 0 in spring equilibrium length. a, b, and c are spring length components in local coordinate system.

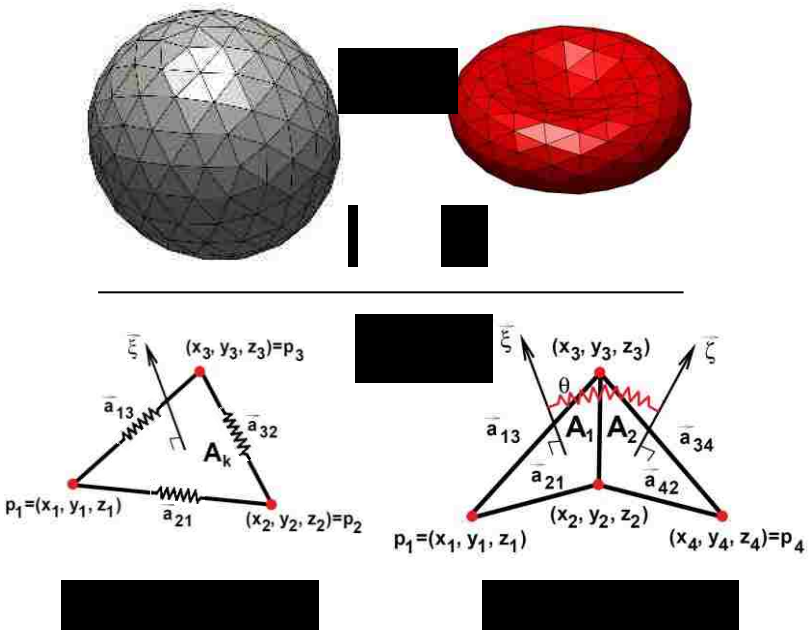

Figure 2.4. (a) Spring connected network cell membrane model. (b) Kinematics for local stretching and bending modes of response.

2.6 Cilia array

Cilia diameter is negligible compared to its height. Therefore, Point-Particle LBM (PPM) scheme can be used to model the micromechanics of these elastic filaments[130]. Via a network of harmonic springs, PPM characterizes an elastic body formed by a chain of regularly spaced beads where the first bead in the chain ($i = 0$) is tethered to the wall ($y = 0$). The elastic energy associated with the chain is[106]

$$U^{chain} = \sum_{i=1}^{N} \left(\frac{1}{2}\right) \left[k_s(|r^i - r^{i-1}| - 1)^2 + k_b(\theta_i - \pi)^2\right] \tag{2.38}$$

where θ_i is the angle between neighboring bonds and k_b represents the cilium bending modulus. The instantaneous angle can be expressed as $\theta_i = cos^{-1}\left(\hat{b}^{\,i+1,i}.\hat{b}^{\,i-1,i}\right)$, where $\hat{b}^{\,i,j} = \left[r^i - r^j\right]/\left|r^i - r^j\right|$, with $\hat{b}^{\,0,1} = j$ being the wall normal direction. Moreover, k_b equals $\pi E r_c^4/4l$ where E is Young's modulus, l is cilium length, and r_c is cilium radius. The hydrodynamic coupling between the fluid and the cilia is captured through a frictional force that is proportional to the slip velocity between the beads and fluid. Namely, the force on the ith cilium bead is given by $F_i^H = -6\pi\eta r_c\left(\dot{r}^{\,i} - u(r^i)\right)$ where $\dot{r}^{\,i}$ is the velocity of ith particle and $u(r^i)$ is the interpolated fluid velocity at position r^i of the particle i. To conserve local and global momentum in the system, an equal and opposite hydrodynamic coupling force is interpolated onto the fluid lattice. In biological cilia, the beating starts from the bottom to the tip. In biomimetic cilia, the actuation force can be originated from either a body force acting on whole cilium or local force at the tip of cilium where concentration of magnetic particle is highest. The difference is the small variation on cyclic motion of cilia which is not the focus of this study. Therefore, for simplicity the cyclic actuating force is applied to the three points at the extreme tip of each cilium. Thus, a periodic force with functional form of $F^{ext}(t) = F_x^0\cos(\omega t)\,i + F_z^0\sin(\omega t)$ is applied at the cilia tip where ω is the frequency of actuation. The beating pattern is symmetric and the actuation force oscillates harmonically in $X - Z$ plane. Finally, it should be noted that the positions of the cilium beads are evolved via a Velocity Verlet algorithm.

2.7 Fluid structure interactions

Fluid structure interaction (FSI) is very important in multiphysics problems, such as bridge design, aircraft design, blood flow in heart, and wind turbine. Numerical method has been

developed to couple the fluid and structure dynamics. Currently there are two general approaches to model FSI problems, e.g. Arbitrary Lagrangian Eulerian method and Immersed boundary method (IBM). In this approach, the fluid mesh conforms to the mesh of solid and on the fluid-solid interface, the velocity and stress should be continuous. As solids are subjected to large translation and rotations, re-meshing is usually used to avoid mesh distortion or entanglement. However, the mesh regeneration is a computationally intensive task. On the contrary, Immersed boundary method (IBM) is a non-boundary fitting method where two independent, overlapping meshes are used for the fluid and solid. It is worthy to mention that IBM approach eliminates the re-meshing procedure and is very efficient in FSI modeling.

Immersed Boundary coupling scheme (IBM) is suitable for fluid-soft structure interaction such as cells and particulate flow, and is well developed in our previous studies [64-68]. The fluid is solved on an Eulerian grid which does not conform to the solid mesh. A force density is applied to the fluid in order to represent the effect of immersed solid boundary

$$\rho\left(\frac{\partial u}{\partial t} + u.\nabla \mathrm{u}\right) = -\nabla \mathrm{p} + \mu\nabla^2 u + f \qquad and \qquad \nabla.\,\mathrm{u} = 0 \tag{2.39}$$

The immersed cell is treated as a parametric surface $X(s,t)$, then the force exerted by the cell structure on the fluid is spread as a source term into the momentum equation. Similarly, the solid velocity will be interpolated from the local fluid nodes. In other word, IBM is used to transfer force and velocity data back and forth between LB (fluid) and SN (cell model).

$$f(x,t) = \int F(s,t)\delta\big(x - X(s,t)\big)ds,$$
$$u(X,t) = \int u(x,t)\,\delta(x - X(s,t))dx \tag{2.40}$$

where $F(s,t)$ is the structural force at location s at time of t, ds is the discretized length of the immersed structure. The force is spread to the local fluid nodes through a delta function $\delta(r)$,

$$\delta(r) = \begin{cases} \frac{1}{4}\left(1 + \cos\left(\frac{\pi r}{2}\right)\right) & -2 \le r \le 2 \\ 0 & otherwise \end{cases} \tag{2.41}$$

In the next chapter, we will first try to validate our cell model by stretch test and then by studying RBC dynamic in shear flow, we can benchmark LBM and IM methods.

Chapter 3: Method Validation

3.1 Cell model benchmark test with optical tweezer experimental results

Network spring model should be able to capture cell mechanical properties and deformation. One of the standard validation method for NS model is the stretching test. In experimental setup, optical tweezers were used to apply force to the RBC membrane at the opposite ends. The longest diameter and transverse diameter were then measured when the cell reached a steady state [104]. Following optical tweezer experiment performed by Mills et al. [131], the deformation of RBC undergoing a dynamic load of 0–200 pN is characterized in order to validate our erythrocyte model. 5120 triangular elements are used to mesh RBC membrane. The bending stiffness, local area constraint, global area constraint and volume constraint constants are chosen as $2.77 \times 10^{-18}\ \frac{kg.m^2}{s^2}$, $23.1 \times 10^{-5}\ \frac{kg}{s^2}$, $4.72 \times 10^{-6}\ \frac{kg}{s^2}$ and $249\ \frac{kg}{m.s^2}$, respectively. The POW (repulsive power function potentials) force coefficient and the persistence length for 27,344 spectrin elements are chosen as $1.66 \times 10^{-27}\ N.m^2$ and $14.68\ nm$ which are scaled for 5120 mesh elements in

our case [62]. To eliminate any residue membrane stress at equilibrium state, nodes were allowed to move on RBC biconcave surface to minimize in-plane energy before starting the simulation. In this stress free condition, the membrane is relaxed and equilibrium lengths of springs are recalculated. More detailed information about spring network model can be found in literature [62]. The stretching test is performed when pair forces are applied at 2% of mesh nodes at either sides of a RBC. As illustrated in Figure 3.1, the curve on the top is the longest diameter along the stretching direction, the curve at the bottom is the cell transverse diameter in the direction perpendicular to stretching. It can be seen in Figure 3.1 that our results for axial and transverse diameters of the deformed RBC are well within the experimental error of Mills et al. [131]. It also agrees well with studies by Fedosov et al. [132] and Pivkin and Karniadakis [133].

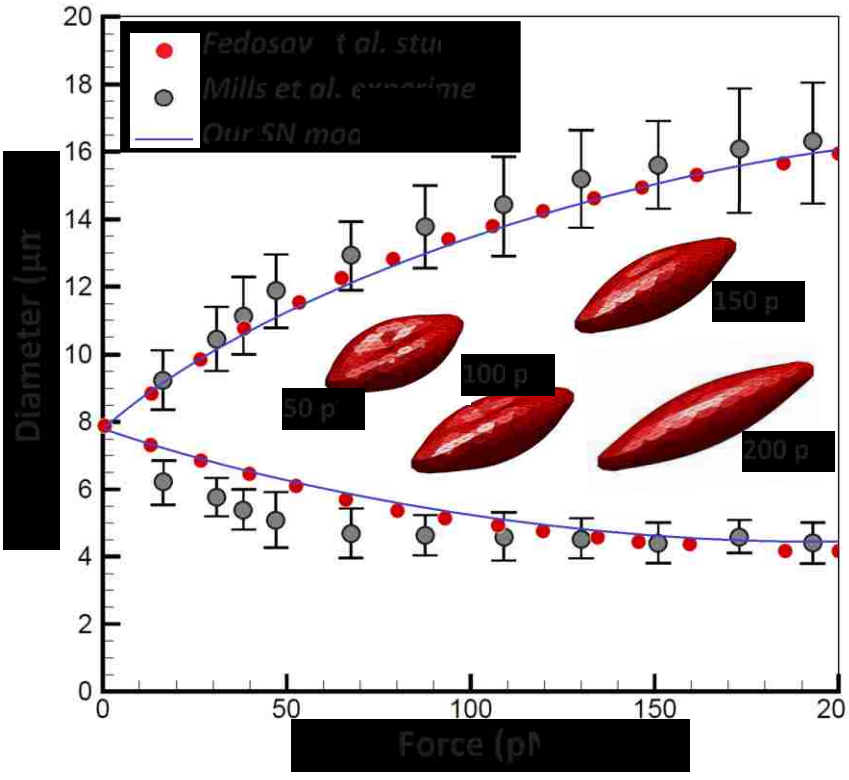

Figure 3.1. (a) The axial and transverse diameters of RBC deformed under stretching test.

3.2 FSI benchmark test by simulating RBC in shear flow

In our in-house FSI code, Immersed Boundary Method is used to transfer force and velocity data back and forth between LB and SN. SN model of RBC in plasma can be benchmarked with experimental data of wheel configuration, parachuting and shear tests. In shear test, tumbling and tank treading motion of RBC when floated in viscous dextran is the focus of study. In this dissertation, to present test cases where the particle deformation is coupled with the fluid flow, the deformation of RBC under pure shear flow is investigated. It is known that at rest, RBCs aggregate into a coin stack shape structure called rouleaux [134]. In shear flow with low-shear rate ($\dot{\boldsymbol{\gamma}}$), rouleaux break and cells tumble while preserving their biconcave shape. As the fluid shear rate increases, the tumbling gradually reduces and RBCs deform into ellipsoidal shape. Tank-treading motion occurs at $\sim 1\ s^{-1}$ where RBC major axis aligns with the flow [135]. In this regime, the membrane starts to rotate around the cytoplasm. In higher shear flows, erythrocyte membrane is dilated. It is believed that RBC reaches its 6% global areal strain limit as shear rate approaches $42{,}000\ s^{-1}$. Below this critical shear rate, RBC can completely recover its biconcave shape when the loading is removed [136].

Abkarian et al. [137] experimentally demonstrated tumbling, tank treading, and intermittent behavior of suspending RBCs in a viscous solution of dextran. Following Pivkin and Karniadakis [133] work, deformation of RBC under pure shear flow is studied when floated in dextran. The viscosity of dextran and intracellular fluid are assumed 22cP and 6cp, respectively. The oscillation period in low shear rates is plotted out in Figure 3.2 where a good agreement with the Abkarian et al. [137] experimental study is achieved. The

flow fields surrounding tumbling and tank treading RBC are also demonstrated in Figure 3.2. The transition from tumbling to tank treading motion is observed at ~1-1.5 s−1 shear rates. We have also calculated tank-treading frequency of RBC under high shear rates ranging from $4{,}000s^{-1}$ to $42{,}000s^{-1}$. Our results indicated that oscillation period is inversely correlated with shear rate as suggested in Fischer's experimental study [138]. Fitting our simulation data, we could link oscillation period to shear rate by following formula, $\omega = \frac{6.3\times10^{4}}{\dot{\gamma}}$.

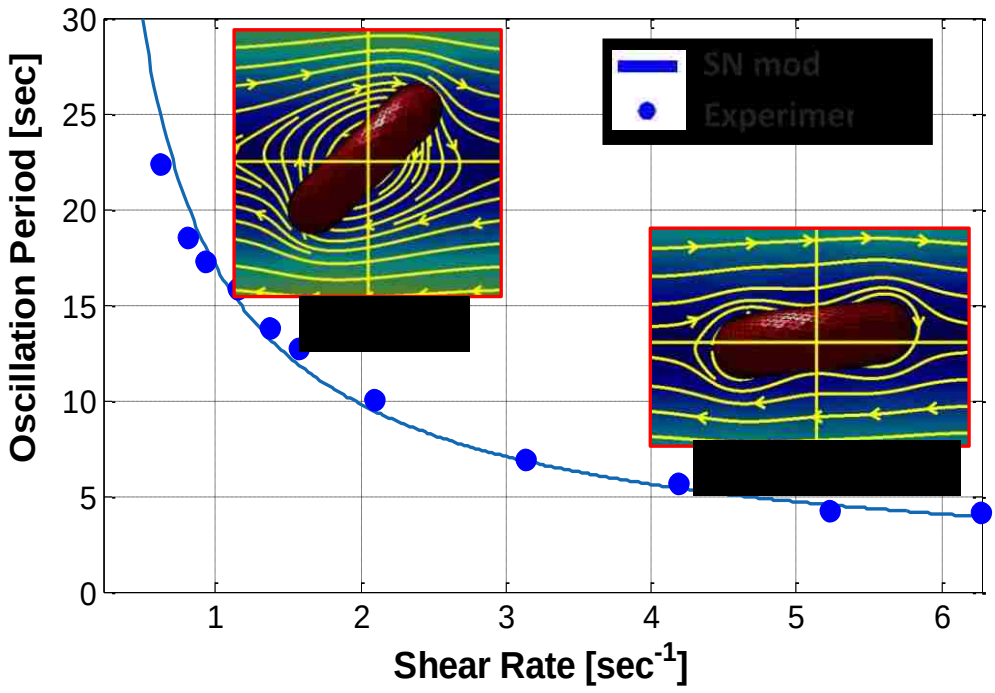

Figure 3.2. (a) Oscillation period over different shear rate for a RBC in shear flow, comparison of our model and experiment.

3.3 Cilia deflection in flow

To benchmark the dynamic of cilia in channel flow, we tried to follow Bhattacharya et. al's works [106, 107]. In that study, they used point particle model (PPM) to study the

interaction of soft microscopic particles motion and active adhesive cilia. It should be noted that in PPM the force density is directly spread on lattice nodes through immersed boundary and this method can only simulate the deflection of high aspect ratio cilia. In contrary, there is another alternative approach for modelling cilia which is called lattice spring model (LSM) and does not have this limitation. In this method, no-slip conditions is explicitly imposed at cilium's surface. Compared to LSM, PPM has considerably lower computational cost and that is the reason we chose PPM for our computationally intensive modelling study. Readers can refer to Bhattacharya et. al's study [106, 107] for more detail information. In this work, PPM and LSM models have been carefully studied.

To benchmark our PPM model, we validated our cilia model with analytical solution proposed by Wexler et. al.[139] where they have developed a mathematical model for deflection of confined fibres. In their proposed equation, deflection and flow rate have linear relationship at low flow rates. The slope of flow rate-tip deflection profile is reported as

$$u \sim u_1 \left(\frac{h}{H}\right) \left[\frac{6\mu(D+d)H^4}{EID^3}\right] Q \tag{3.1}$$

where E is Young's modulus; d and I are cilia diameter and moment of inertia; u_1 is a function of $c = h/H$; $H$and D are is channel height and width, respectively. They did an experimental study to validate their model. In their setup, it should be mentioned that the longest rectangular shape cilia tested had the dimension of $22\mu m \times 56\mu m \times 241\mu m$ and therefore, the largest the length to diameter aspect ratio is ~ 6. To ensure cilia can properly reproduce drag coefficient for flow normal to the filaments, we examined the flow of fluid

past an elastic fibre in a channel with dimensions of $L_x = 80\mu m, L_y = 10\mu m,\ L_z = 40\mu m$. It is observed that our cilia model agrees well with analytical solution at moderate flow rates as shown in Figure 3.3. However, at low flow rates our model predict a nonlinear relation between cilia tip deflection and flow rate. Discrepancy is due to cilium aspect ratio of 20 used in our simulation as opposed to highest aspect ratio of 6 used in[139]. In the next section, we will briefly discuss damage to RBC as it undergo critical deformation.

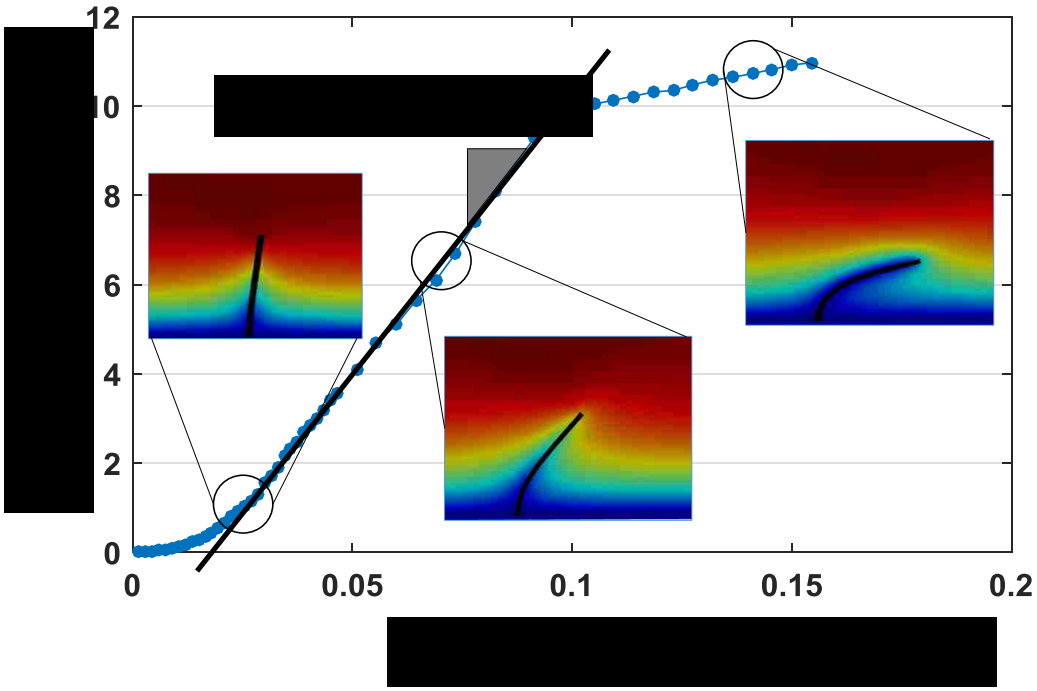

Figure 3.3. Cilia tip deflection, u_y, versus flow rate, Q, for $H = 40\mu m$, $D = 10\mu m$, $h = 13.3\mu m$, $E = 0.132Mpa$, $d = 0.66\mu m$, and $u_1(13.3/40) = 6.1 \times 10^{-4}$.

3.4 Introduction to RBC damage

Red blood cell take a bullet shape when squeezing through a pore smaller than its diameter as shown in Figure 3.4. Flow rate and initial orientation of RBC influence its dynamics. Higher flow rate results in higher stress level. The highest shear stress level on RBC

membranes happens in the necking region at the mid-section of the bullet shaped RBC, as shown in Figure 3.5a. The regions of concentrated stress might have pore formation/growth as shown in Figure 3.5b.

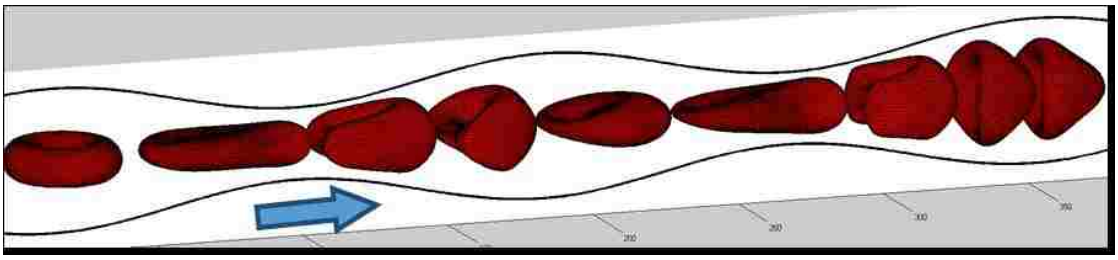

Figure 3.4. Red blood cell dynamic squeezing through a pore.

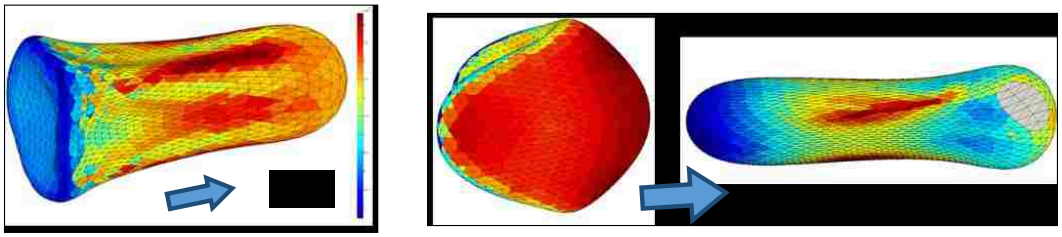

Figure 3.5. (a) shear stress distribution on RBC membrane; (b) a damaged RBC flowing through a shrinking channel; the arrows indicate the flow direction.

Our first step toward studying damage in mesoscale is modeling a damaged RBC under shear flow. Based on stress distribution on membrane, we can estimate damage and hemolysis which will be explained in detail in the next chapter. To better capture pore growth, a much denser local mesh at damaged regions is needed. Thus, the mesh size will be locally decreased to actual spectrin size (~75nm) and accordingly the stress/strain data on spectrin level mesh can be directly used in CGMD model. It is also worthy to mention that in narrow channels RBC will deform into parachuting shape as it comes out of nozzle head, see Figure 3.6.

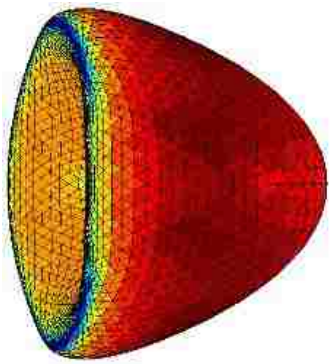

Figure 3.6. Parachuting shape of RBC in a narrow channel.

Lattice Boltzmann method's particulate nature makes it very suitable for large scale parallel computing to handle a large number of RBCs[140]. Currently, our in-house code can handle different fluid properties inside/outside of RBC since the hemoglobin/plasma viscosity can influence RBC dynamics. Our code also enables local adaptive meshing at critical solid and fluid domains. Moreover, a connectivity matrix stores the network information in our in-house code and based on our proposed model, we can implement unfixed spectrin network connectivity which can actively experience remodeling under a certain level of shear deformation. However, in this dissertation, we did not need to do that since we only focused on RBC damage under shear flow. In the net chapter, we will first describe the details of our multiscale damage model and then evaluate shear induced damage.

Chapter 4: Multi-scale Modeling of RBC Hemolysis

4.1 RBC rupture under stretching load

Spectrin network is the main load bearing component of membrane. Therefore, spring forces are the dominant terms in calculating stress components compared to bilayer hydrostatic elastic force. Using Equations in Chapter 2, stress distribution on erythrocyte membrane is calculated and plotted out in Figure 4.1 when RBC undergoes the stretching test. The regions close to the gripping ends are identified as critical regions with highest stress level where the membrane is more likely to be damaged. Finer triangular mesh with the sizes comparable to the size of spectrin tetramer is needed for studying the damage initiation and growth in these regions. Thus, smaller mesh is generated locally by splitting every triangular element into four so that the size of mesh is similar to spectrin size, ~75nm, as shown in Figure 4.1. Using this approach, mesh can be refined dynamically and simulation can be performed with minimal computational costs compared to uniform spectrin mesh.

The maximum pulling force in optical tweezer experiment is 200pN where RBC can completely recover its biconcave shape when the loading is removed. It is observed that the stretching force on critical tetramer, the spring with highest force, changes linearly with pulling force as shown in Figure 4.2. According to CGMD study of Li et al. [60], actin-spectrin association is breakable at 10.9% bond strain which corresponds to 24.9 pN force. In the same study, it is mentioned that the strength of dimer-dimer association is known to be much weaker than the actin-spectrin association, but this disassociation force is not explicitly reported. In high pulling forces, some spectrin network bonds close to gripping ends break first. Then, rupture initiates at the tip of the damaged region which ultimately leads to fragmentation of RBC membrane as shown in Figure 4.**3**.

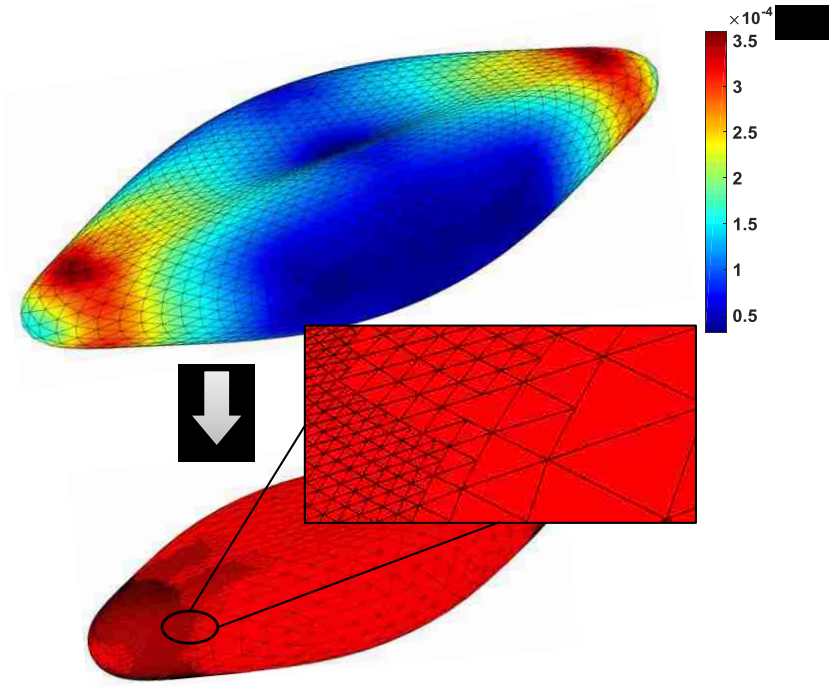

Figure 4.1. Stress distribution and adaptive Spectrin level mesh generated locally in critical regions.

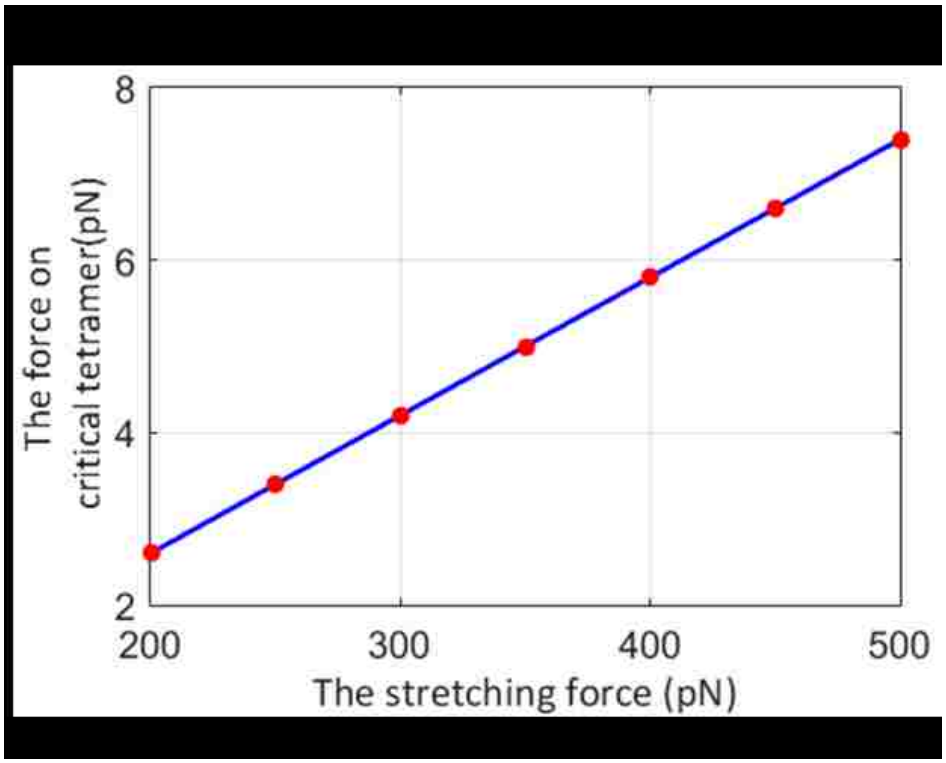

Figure 4.2. Force on critical tetramer as RBC is stretched with various pulling forces.

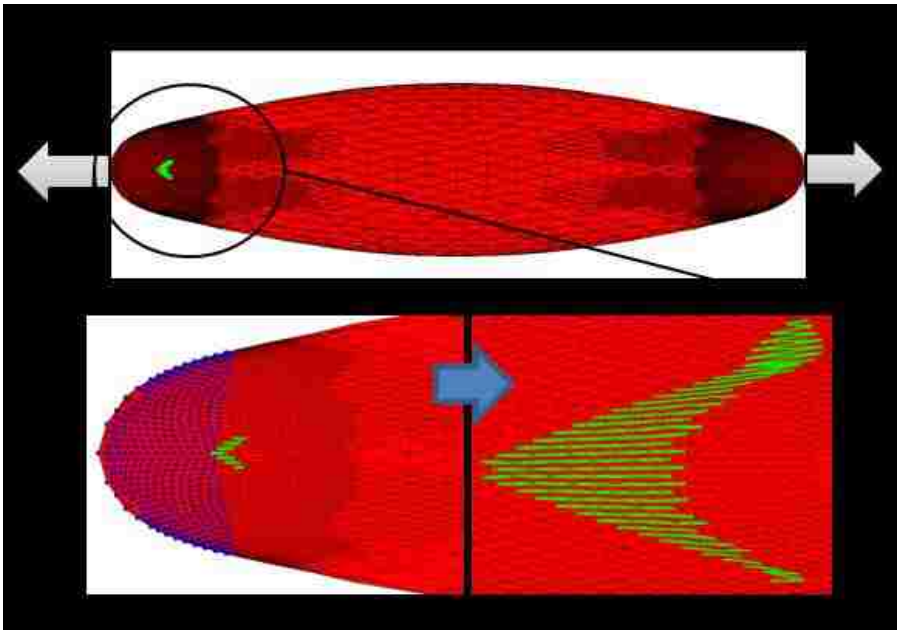

Figure 4.3. RBC rupture under high stretching forces.

4.2 RBC deformation under shear flow

The membrane continuously undergo cyclic stretch loading during RBC tank-treading motion. Moreover, stress/strain distributions on membrane also change during oscillation period because of RBC's at-rest biconcave shape. In other words, tetramers in Spectrin network may experience different stretch loading depending on where they are originally located on membrane. It is shown in Figure 4.4 that the maximum force on critical tetramer almost linearly increase with shear rate and reaches $\sim 8.3\ pN$ in $42{,}000\mathrm{s}^{-1}$. At critical shear rate of $42{,}000s^{-1}$, the membrane stress level is significantly increased and RBC is stretched to twice of its original diameter as shown in Figure 4.4 and Figure 4.5. In shear rates above this threshold, irreversible damage to Spectrin network and fragmentation of RBCs leads to significant increase in free hemoglobin content of the suspending medium [29].

Formation of pores in regions with critically high areal strain during sublytic hemolysis allows limited release of hemoglobin molecules. It should be noted that the maximum local areal strain of membrane varies from 75% to 120% under shear rates of $4{,}000 - 42{,}000\mathrm{s}^{-1}$ as shown in Figure 4.5. Koshiyama and Wada [57] showed that nanopores begin to form on lipid bilayer membrane at 85% areal strain. Moreover, another MD study by Tomasini et al. [141] showed that in quasistatic shearing tests of lipid membrane, pores begin to form at $\varepsilon_A = 80\%$. Thus, our findings agrees with these CGMD studies since sublytic hemolysis also starts at $4{,}000\mathrm{s}^{-1}$ with maximum areal strain of 75%. In the following section, the sub-models for evaluating sublytic damage will be discussed.

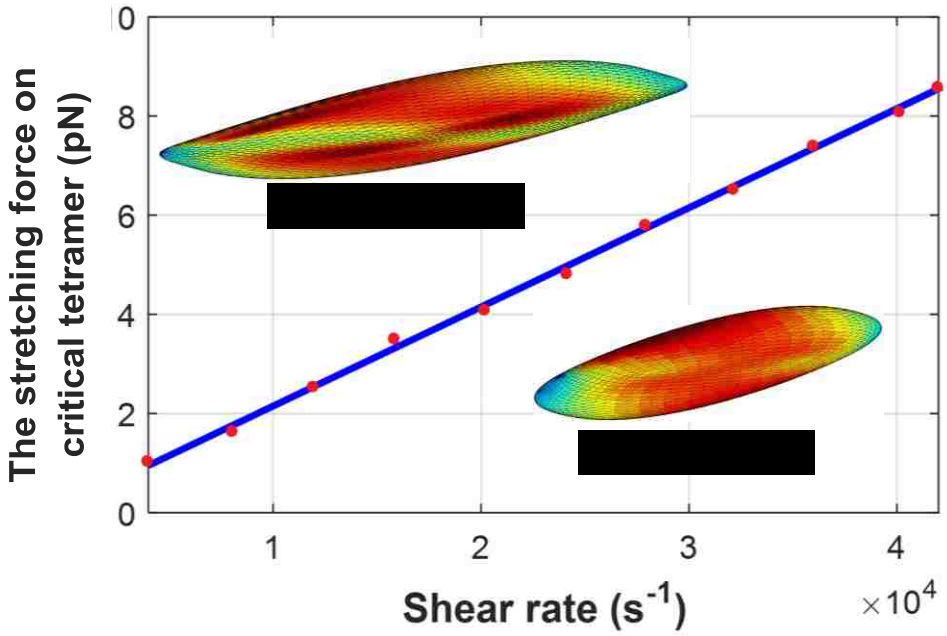

Figure 4.4. Maximum force on critical tetramer under various shear rates.

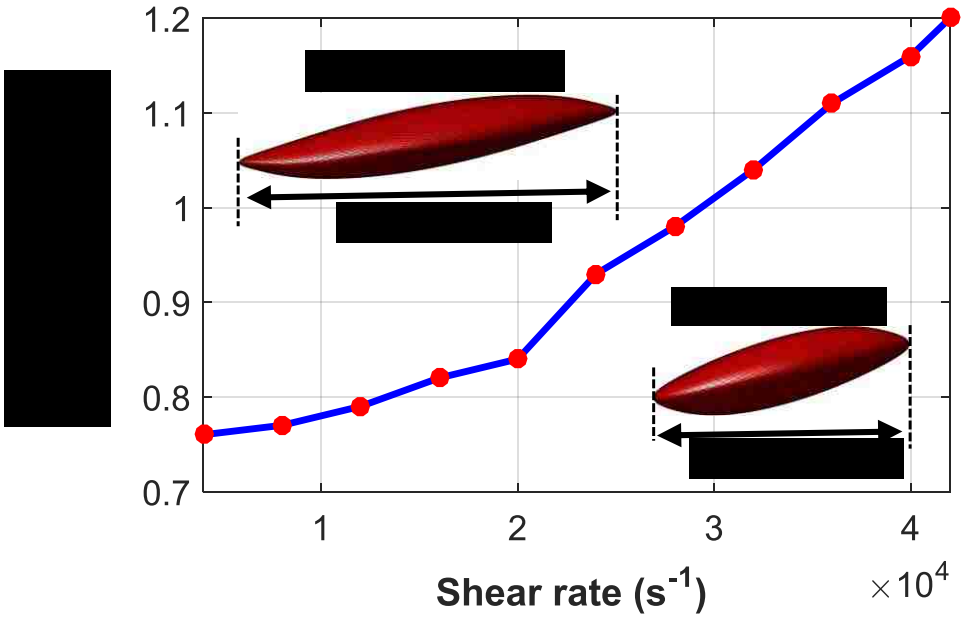

Figure 4.5. Maximum local areal stain on RBC membrane versus shear rate.

4.3 Dynamics of RBC damage

Since cell rupture is very difficult to be observed directly, hemoglobin is used as indicator for post-rupture detection. Hemoglobin can only be released out of cells when the cell membrane is ruptured. Thus, red blood cells damage can be correlated to the hemoglobin level inside the cell or free hemoglobin in the blood serum. Each RBC contains about 280 million hemoglobin molecules. The globin protein has 4 subunits (2 alpha and 2 beta) and each subunit has one heme group. Hemoglobin has a fiber like structure with dimensions of 10 nm by 1 μm when it is stretched [142]. Its fiber structure is typically entangled together and be modeled as a single bead[143] following a hemoglobin model reported in literature[144], as shown in Figure 4.6. Since it is computationally expensive to track all the hemoglobin individually, diffusion-convection equation will be used to model Hb release.

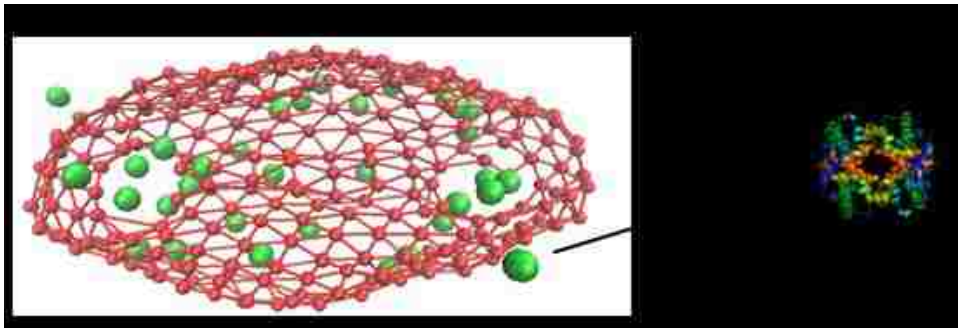

Figure 4.6. Hemoglobin release from ruptured cell membrane where hemoglobin are modeled as beads

The onset of pore formation initiates the release of intracellular content into plasma. The membrane dilates to 6% of its original size under $42{,}000\mathrm{s}^{-1}$ shear flow while local areal strain at critical sites can even reach 120% under the same flow condition. To the best of our knowledge, all previous strain-based hemolysis studies are based on global areal strain

[49, 51, 52, 56]. However, it is necessary to study sublytic damage locally due to complex loading dynamics of erythrocyte membrane under shear. Our sublytic damage model is based on hindered Hb release out of pores formed in critical regions. It is indicated that below $42{,}000\mathrm{s}^{-1}$ shear rate, spectrin network is less likely to be damaged irreversibly. Thus, it is hypothesized that pores do not grow bigger than spectrin length, ~75nm, during sublytic damage. In literature, researchers have been using dyes with different molecular size to study diffusion process through nanopores [145], specifically to determine the cut off diameter of pores that are being created in lipid bilayer membrane [146]. In our modeling study, these nanopores are assumed to form instantly due to the relatively small time scale of pore growth ($\approx 10\mu s$) [147] compared to the oscillation period of RBC ($\approx 1-6ms$). In the following, we will first discuss the dynamics of pore formation and the method we applied to implement it in our damage model.

4.4 Pore formation in critical regions

Pore formation at the molecular level is a statistical phenomenon [57]. Thus, the probability of pore formation in critical regions needs to be implemented into our damage model. Many researchers have performed MD simulations of pore structure in the bilayers [141, 148-150]. Koshiyama and Wada [57] specifically studied pore formation dynamics under various stretching speeds. They performed equibiaxial stretching simulations on a 40×40nm bilayer patch with pulling speeds, c, of 0.1, 0.3 and 1.0 $m.s^{-1}$. Their MD simulation results indicated that multi-pores are more likely to form under high stretching speeds. They also performed quasistatic (QS) stretching test where just a single pore was created [57]. It is described before that the oscillation period of RBC varies from 15 to $1.5ms$

under 4,000 and 42,000 s^{-1} shear rates, respectively. To calculate the membrane stretching speed under high shear rate flows, the RBC surface is hypothetically divided into 40 × 40 nm patches where they continuously undergo cyclic loading with oscillation period of 1.5ms. Assuming maximum 120% areal expansion, the pulling speed in critical patches can be estimated as 10 $mm.s^{-1}$ which is much lower than $c = 0.1\ m.s^{-1}$ in Koshiyama and Wada [57] study. Thus, it can be concluded that the membrane stretch ca be considered as quasistatic in extreme cases of sublytic hemolysis.

To present the average chance of pore formation as a function of areal strain, Koshiyama and Wada [57] used an error function to demonstrate the ratio of patches containing pores to total number of patches. It can be expressed as $R(\varepsilon_A) = \frac{1}{2}\left[1 + erf\left(\frac{\varepsilon_A - \overline{\varepsilon_A}}{\sqrt{2}\sigma}\right)\right]$, where $\overline{\varepsilon_A}$ and σ are the mean and variance of critical areal strain, respectively. Their results for quasistatic stretching case are fitted by Gaussian distribution function with mean and variance of 1.04 and 0.07, and is used to calculate the probability of pore formation in this study as shown in Figure 4.7.

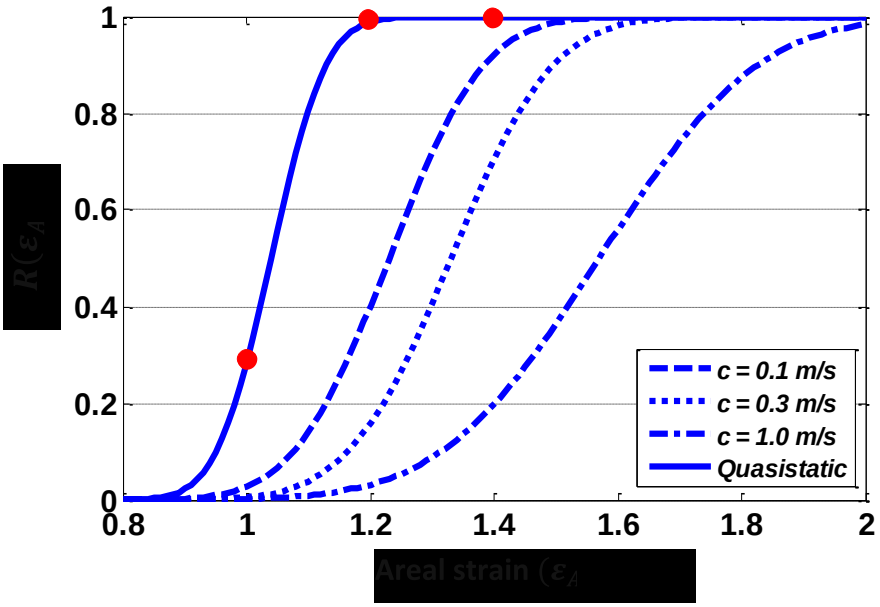

Figure 4.7. The probability of pore formation $\boldsymbol{R(\varepsilon_A)}$ and its corresponding normal distribution for various stretching speeds [57].

4.5 Hemoglobin transport through nanopores

The so-called sublytic phase of RBC damage occurs when pores are large enough to allow Hb to scape. The Hb flux out of a single pore can be calculated as [56]

$$\frac{dHb_p}{dt}V_p = \sum_{pores} D_{eff}\frac{\left(Hb_{RBC} - Hb_p\right)}{L}A_{pore} \tag{4.1}$$

where Hb_{RBC} and Hb_p are the intracellular and plasma Hb concentrations, respectively; V_p is volume of plasma; D_{eff} is effective diffusion coefficient of Hb out of nanopores and A_{pore} is pore opening area. V_p, Hb_{RBC}, and index of hemolysis (IH) are expressed as

$$V_p = \frac{1-Hct}{Hct}V_{RBC}; \qquad Hb_{RBC} = \frac{Hb_B}{Hct} - \frac{(1-Hct)Hb_p}{Hct}; \qquad IH = \frac{Hb_p - Hb_p^0}{Hb_B} \tag{4.2}$$

where Hb_B and Hct are blood Hb concentration and hematocrit, respectively. Using Eq. 1, Eq. 2 can be rewritten as:

$$\frac{dIH(t)}{dt} = \frac{1}{(1-Hct)V_{RBC}}\left(1 - IH(t) - \frac{Hb_p^0}{Hb_B}\right)\sum \frac{D_{eff(r_{pore})}}{L(\varepsilon_A)} A_{pore}(\varepsilon_A) \tag{4.3}$$

Assuming zero initial plasma free hemoglobin concentration (Hb_p^0), IH level can be calculated using effective diffusion, pore opening area, and membrane thickness. These parameters depend on local loading condition of bilayer membrane. In what follows, these parameters are discussed in details.

4.6 Pore size and length

One important part of our damage model is estimating the membrane thickness and pore size as a function of areal strain. Tolpekina et al. [148] used coarse grained MD to stretch a bilayer patch up to 1.7 of its equilibrium area. They established the phase diagram of pores and identified regions where pores are stable. Based on these findings, they also proposed a simple theoretical model to correlate pore radius, R_{pore}, and area strain by minimizing free energy. It is expressed as

$$R_{pore} = 2\left(\frac{A-A_0}{3\pi}\right)^{1/2} cos\left(\frac{\alpha}{3}\right); \qquad \cos(\alpha) = -\frac{k_c}{2K_A}\frac{A_0}{\pi}\left(\frac{A-A_0}{3\pi}\right)^{-3/2} \tag{4.4}$$

where A_0 is the area of the tensionless membrane without a pore; $K_A = 250\, mJ.m^{-2}$ is the compressibility modulus of membrane; and k_c is the line tension coefficient which is equal to 3.5×10^{-11} J/m. The average pore radius in 40×40nm patch as a function of relative

areal stretch is demonstrated in Figure 4.8. Moreover, the membrane thickness decreases as membrane stretches. Koshiyama and Wada [57] also demonstrated how membrane thickness at porated regions change by areal strain which is directly implemented into our model.

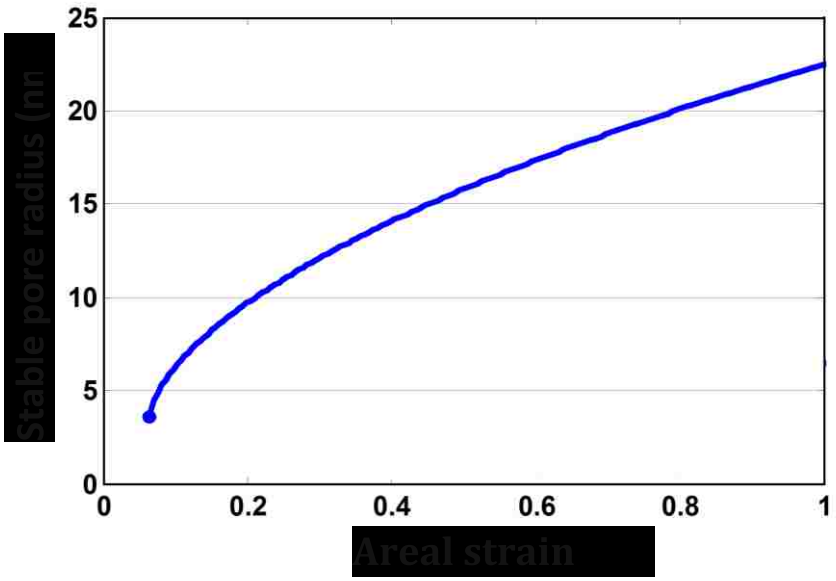

Figure 4.8. The stable pore radius under various areal strain for 40×40nm [148] patches.

4.7 Hb Diffusion out of nanopores

Hemoglobin is the main component of the red blood cell. A RBC approximately contains 280 million hemoglobin molecules with molecular size of $6 \times 5 \times 5nm$ [151]. Hemoglobin in erythrocyte is highly concentrated, 330 mg/ml under physiological conditions. It occupies a quarter of a cell volume where the average separation distance between its molecules is 6.9nm. Due to Hb high concentration inside RBC, its self-diffusion coefficient is six times smaller compared to that in dilute solution [152]. An exponential function is proposed by Moreno and Wittenberg [153] to demonstrate

correlation between Hb concentration and diffusion coefficient. Significant reduction in Hb diffusivity is attributed to obstruction effects by excluded volume interactions. Doster and Longeville [152] experimentally estimated the self-diffusion coefficient of hemoglobin in RBC as $1.75 \times 10^{-7}\ cm^2/s$ while its diffusion coefficient in dilute solution is reported as $8.61 \times 10^{-7}\ cm^2/s$.

During sublytic hemolysis, Hb diffuses out of temporary small nano-pores. The effective diffusion coefficient of these macromolecules through pores of comparable size is usually much lower than their value in bulk solution. Hemoglobin transverse diffusion, known as "hindered" or "restricted" diffusion, is caused in two ways. First, steric and long-range interaction between hemoglobin and pore wall in lipid bilayer tend to exclude hemoglobin from some radial positions within the pores. Second, hydrodynamic drag on hemoglobin molecule is increased due to confined space of the pore [154, 155]. The effective diffusion coefficient of these macromolecules can be expressed in terms of the solute-to-pore size ratio $\lambda = R_s/R_p$ as $\frac{D_{eff}}{D_0} \approx \Phi(\lambda)K^{-1}(\lambda)$ where K^{-1} is ratio of the friction coefficient of the solute in bulk solution to that within the pore [156] and Φ is the ratio of the average solute concentation within the pore to that in bulk solution. Hemoglobin molecules inside RBC are partially flexible and exhibit hydrodynamic behavior similar to coiled chain molecules. The partition coefficient, Φ, of a neutral, randomly coiled macromolecule can be calculated by the analytical expression of Casassa [157]. K^{-1} and Φ are written as:

$$K^{-1} = 1 - 2.848\lambda + 3.269\lambda^2 - 1.361\lambda^3 \tag{4.5}$$

$$\Phi = 4\sum (1/d_i^2)\ exp\,(-d_i^2\lambda_i^2) \tag{4.6}$$

where d_i are the roots of $J_0(d) = 0$, with J_0 representing the Bessel function of the first kind, of order zero. λ_i depends on the permeability parameter which demonstrates the resistance to solvent flow through the macromolecule and can be estimated as $1.3 \leq \lambda_i/\lambda \leq 1.8$. In the current study, λ_i/λ is assumed as 1.8. Furthermore, the classical equation of Stokes-Einstein, $R_s = \frac{kT}{6\pi\eta D_0}$, is used to calculate Hb Stokes-Einstein radius where k is Boltzmann's constant, T is absolute temperature, and η is the solvent viscosity. Finally, using equations above, effective diffusion of Hb through nanopores can be estimated in terms of solute-to-pore size ratio as shown in Figure 4.9.

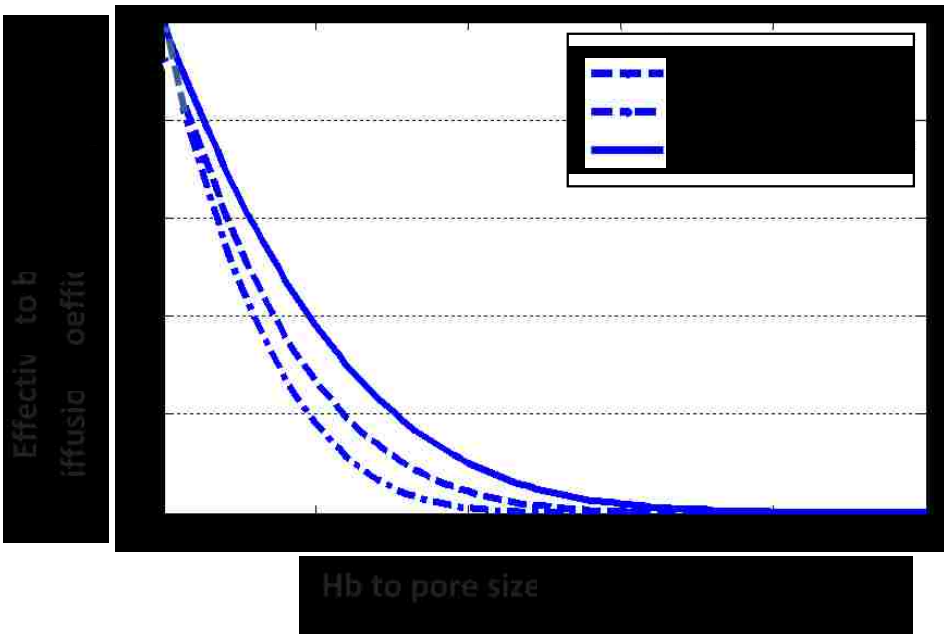

Figure 4.9. The effective diffusion to bulk solution diffusion coefficient over different Hb-to-pore size ratio.

4.8 Algorithm for multiscale model

To incorporate statistical feature of pore formation into our model, erythrocyte membrane is divided into 40×40 nm patches. A critical areal strain threshold, randomly picked

from Gaussian distribution as shown in Figure 4.7, is assigned to each patch. As RBC membrane deforms under shear flow, each patch experiences different loading cycle during oscillation periods. Once areal strain exceeds the specified critical threshold, a single pore will form in the damaged patches. The pore size and length can be calculated using areal strain as described before. It should be noted that the areal strain and accordingly pore size and effective diffusion also change during oscillation period. Finally the pores in damaged patches will be assumed closed as areal strain reaches below 20% when pore size is smaller than Hb molecule. The solution procedure is illustrated in the flow chart shown in Figure 4.10.

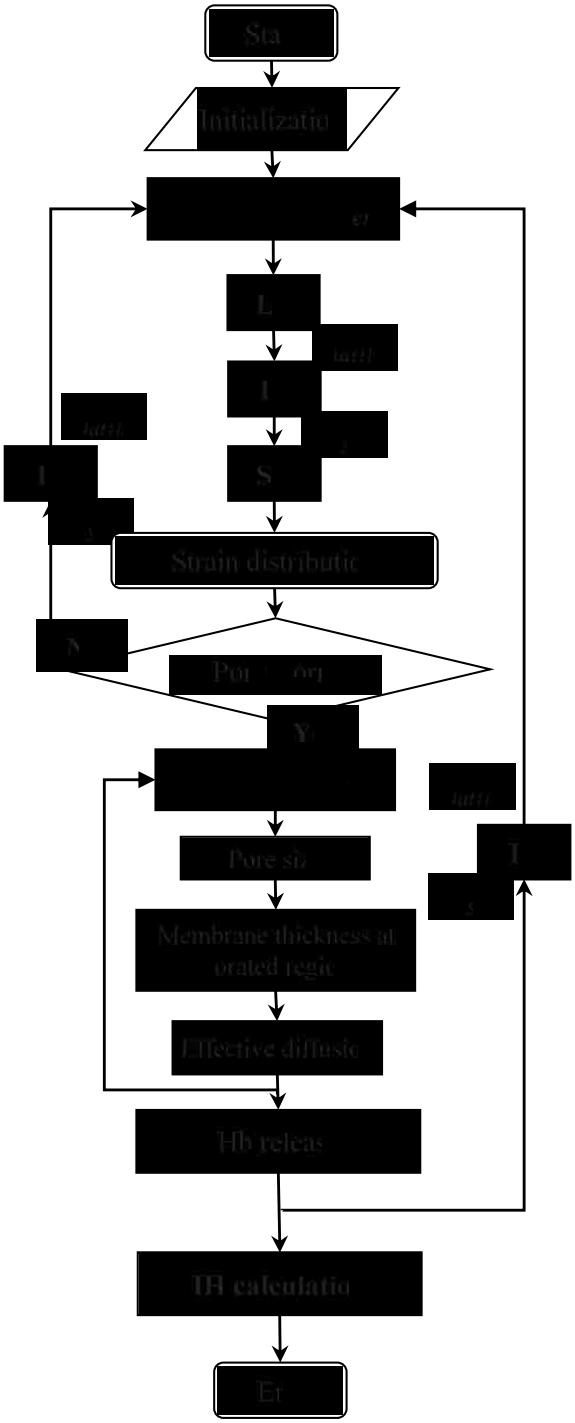

Figure 4.10. Solution process flow chart.

4.9 Hemolysis result

Due to the biconcave shape of RBC, the porated area, shown in Figure 4.11, also fluctuates during oscillation period. The relative pore area changing with oscillation time is plotted out under various shear rates in Figure 4.12. The average relative pore area over oscillation period varies between $0.001 - 0.03$ under shear rates ranging from $14{,}000$ to $42{,}000\ s^{-1}$. Minimizing membrane energy landscape, vitale et al. [56] also estimated $\sim 5.5\%$ relative pore area under a critical shear rate of $42{,}000\ s^{-1}$ when global areal strain is 6%. Although our approach is completely different from their continuum-based method, our relative pore area matches with their prediction. In the same study, pore density and diameter in 6% global areal strain are reported as $111\ \mu m^{-2}$ and 24nm, respectively. It is worthy to mention that pore size in our damage model varies between $\sim 10 - 40\text{nm}$.

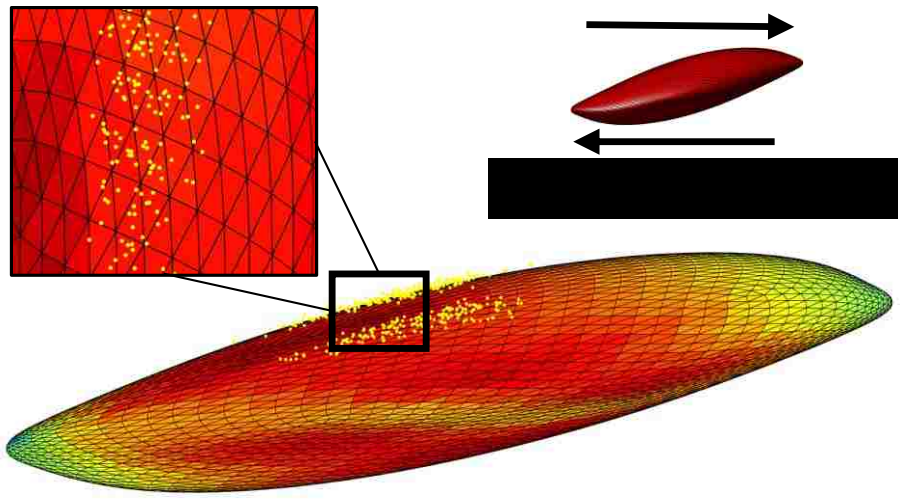

Figure 4.11. Nanopore distribution under RBC membrane under $30{,}000 s^{-1}$ shear flow.

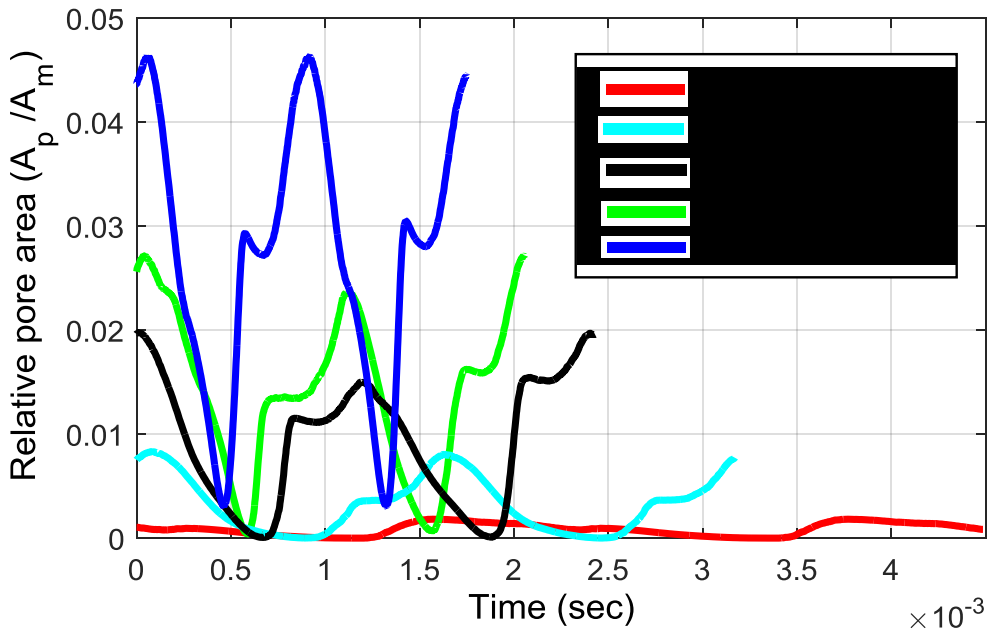

Figure 4.12. Relative pore area fluctuation during oscillation time in different shear rates.

Diffusion of Hb out of nanopores during sublytic damage is hindered by excluded volume interactions. Vitale et al. [56] used hemolysis data from Heuser and Opitz's [158] experiments to propose an exponential function for mass-transport coefficient of hemoglobin across erythrocyte membrane as a function of shear rate. It was expressed as $K_c(\,\mu m.s^{-1}) = D_{eff}/L = 1.67 \times 10^{-8} G_f^{1.54}$ where G_f and L are shear rate and membrane thickness, respectively. They estimated the mass-transport coefficient as ~0.01 to $0.2\,\mu m.s^{-1}$ under shear rates of $4{,}000s^{-1}$ and $42{,}000s^{-1}$, respectively. On the contrary to Vitale et al. [56] study, we calculated Hb mass-transport coefficient individually for each pore since effective diffusion coefficient and accordingly K_c are functions of pore size. Averaging Hb mass-transport coefficient over all pores, it is observed that our damage model predicts that K_c varies from $0.04\ to\ 0.55\ \mu m.s^{-1}$ which roughly agrees with their experimentally estimated range. So far, we presented validation

of our submodels by comparing our results for mass transport coefficient and relative pore area with other studies.

Calculating strain distribution on RBC membrane in every time step, we can accordingly find the location of pores, membrane thickness, pores diameter and effective diffusion as shown in Figure 4.10. Subsequently, Hb flux out of each nanopore is estimated separately using ODE in Eqn(4.3). Finally, we would be able to calculate index of hemolysis during various exposure time. It is shown in Figure 4.13 that our results agrees well with experimental study of Giersiepen et al. [46] under shear rates higher than $20{,}000s^{-1}$. Minor inconsistencies between our prediction and experimental measurement may be attributed to simplified assumptions in our sub-models. For instance, CGMD results from equibiaxial stretching tests are used to determine pore formation criteria while membrane undergoes various loading conditions which are not necessarily equibiaxial; nanopores may not be always circular as it happens in equibiaxial stretching condition; Hemoglobin-lipid bilayer interaction is overlooked for calculation of Hb hindered diffusion coefficient. Moreover, our damage model focuses on Hb diffusion out of a single RBC compared to macroscale estimation of hemolysis in experimental setups.

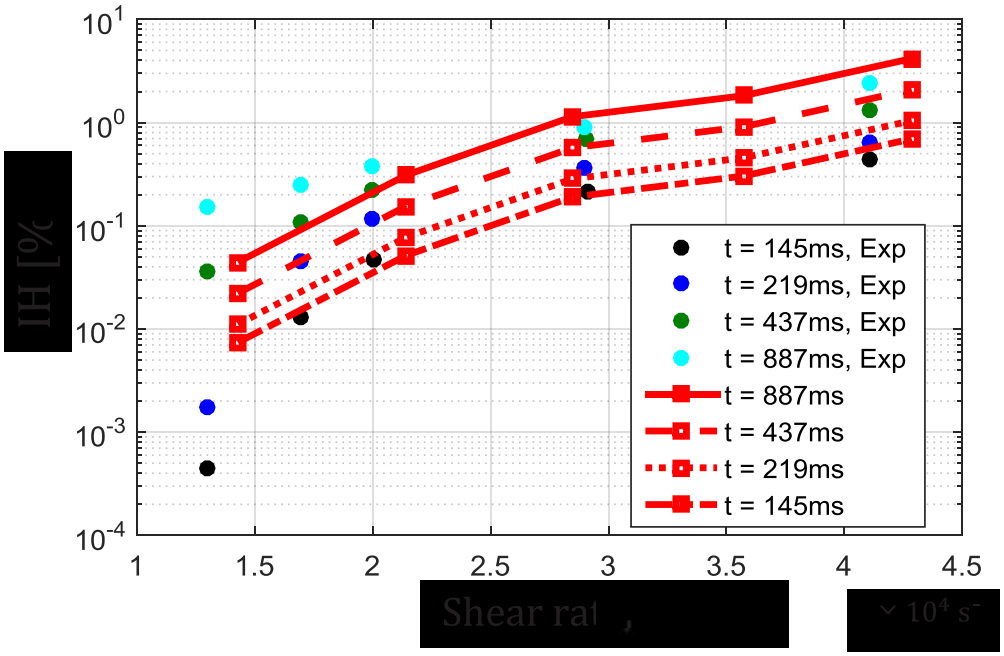

Figure 4.13. Comparison of the index of hemolysis (IH) between Giersiepen experimental data (points) [46] and our damage evaluation (lines).

To better understand different model parameters such as Hb diffusive transport and relative pore area, hemolysis for low IH levels, Eq. 3, can be roughly estimated as

$$IH = \frac{\Delta t\, K_c\, X\, A_{RBC}}{(1 - Hct)V_{RBC}} \tag{4.7}$$

where $A_{RBC} = 135\mu m^2$ and $V_{RBC} = 95\mu m^3$ are initial area and volume of a RBC, respectively; X is relative pore area; and Δt is the exposure time. Giersiepen hemolysis experiments [46] showed that IH level increase to 1% during $\Delta t = 887ms$ exposure time under $30{,}000s^{-1}$ shear rate. Assuming the average relative pore area of $X = 1\%$ under this flow condition (Figure 4.12), K_c can be roughly estimated as $0.43\ \mu m.s^{-1}$ using Eqn(4.7). On the other hand, K_c can be calculated as $\frac{8.61\times10^{-7}\ cm^2/s}{10\ nm} = 8600\ \mu m.s^{-1}$

using normal diffusion coefficient of Hb in dilute solution. This considerable difference is attributed to small size of pores, comparable to size of Hb molecules, which highly restricts diffusion of Hb out of nanopores. Therefore, it seems reasonable to assume that spectrin network confine the growth of pores on lipid bilayer during sublytic damage.

Chapter 5: Soft Particle Sorting Using Bioinspired Synthetic Cilia Array

5.1 2D model

In a straight channel, the coordinated motion of cilia actively change the axial components of velocity near ciliated region. These beating hair-like filaments can even switch the directionality of the net flow[159] and draw or repel away flow particles to/from ciliated region. In these flows, the sperm number quantifies the relative importance of the viscous force compared to the bending rigidity of oscillating cilia. The sperm number can be written as

$$Sp = L(\zeta\omega/EI)^{1/4} \tag{5.1}$$

where $\zeta = 4\pi\upsilon\rho$ is the viscous drag coefficient, $\omega = 2\pi f$ is the angular velocity of the driving force, and EI is the bending rigidity of cilium. For relatively small Sp, the dynamic

of cilium is governed by its elasticity and cilia array is unable to generate net flows at low Re[160]. For high Sp numbers, no net fluid flow is generated due dominant effect of fluid viscosity. Once the cilium elasticity and fluid viscosity forces are of comparable magnitudes, coupling between elastic filaments and viscous fluid can create net flow.

The dynamics of interaction between beating cilia and flow particles is initially studied in 2D. A 2D model provides a better insight into the underlying physics. The dimensions of computational box is 240 × 120 in lattice unit and the periodic boundary conditions are applied at both inlet and outlet while we use body force to replace necessary pressure gradient. The node spacing on particle's membrane is almost equal to one lattice unit and the equilibrium shape of RBC is followed by the analytical curve from Fung[161]. The length of cilium and channel are $l = 13\mu m$ and $L = 40\mu m$, respectively. The intercilium separation in cilia array is $14\mu m$ and the actuation frequency is $120Hz$. The simulation time step is 1.6×10^{-7} where the time period of actuation is T = 50,000 LB time units. In the PPM simulations, the bond length between the point particles has to be approximately 1 LB unit, hence $N_{cilium} = 80$, and the radius of each point particle has to be much less than 1 LB unit for the model to be valid, thus $r_{cilium}/l = 0.016$[106]. The dimensionless values for the relevant parameters used in the simulations are $Re = UL/\nu = 0.2$, Sp = 6, $F_{x0}l^2/EI = 64$ and $F_{z0}/F_{x0} = 4$. First, actuated cilia are simulated without particles and after reaching equilibrium, particles are added to remove the effect of initial conditions on particle transient motion.

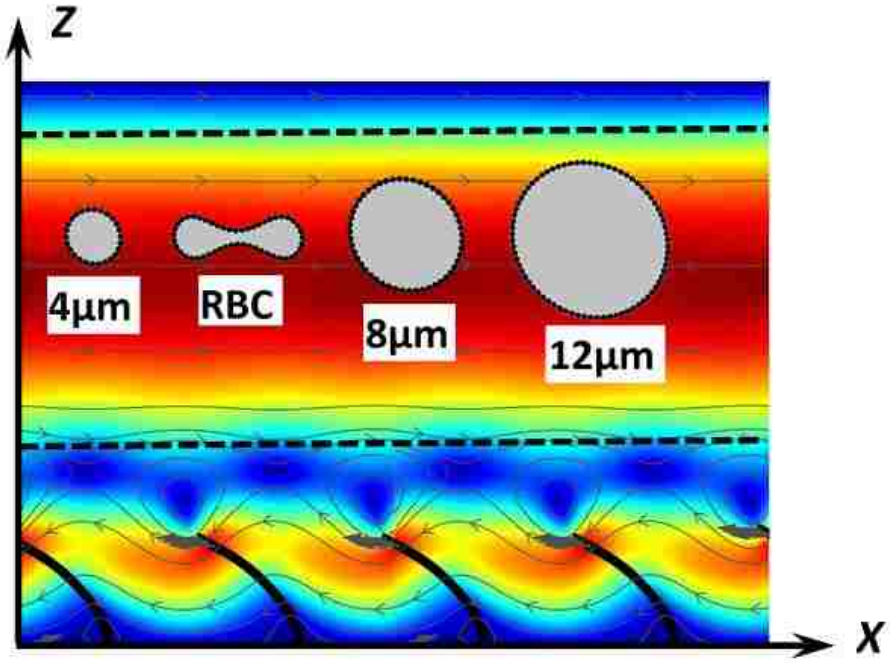

Figure 5.1. 2D particles flowing in channel decorated with cilia array.

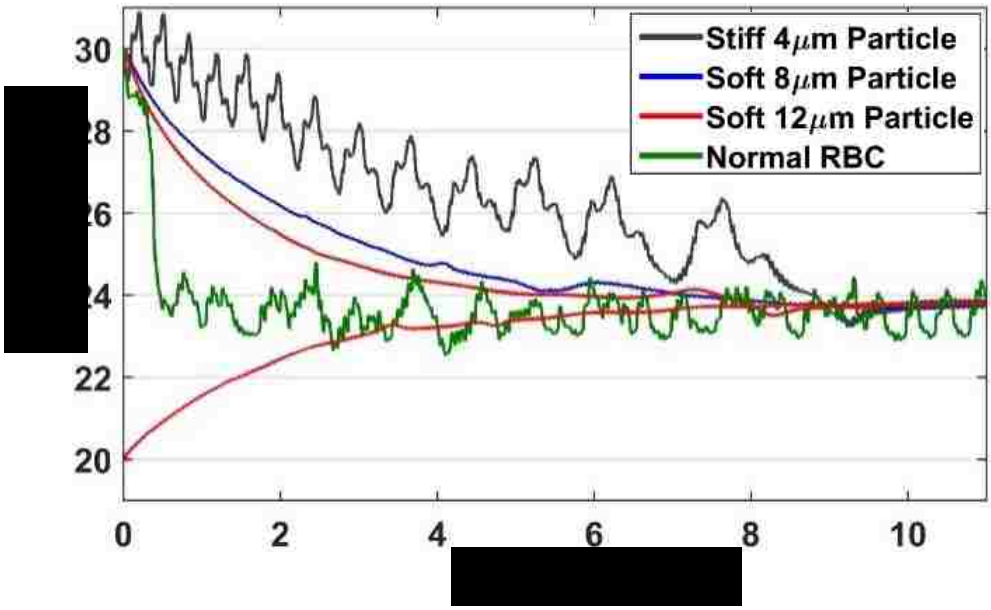

Figure 5.2. Vertical displacement of particles with different size, shape and stiffness due to harmonic actuation of cilia array.

The deformability of cancer cells varies a lot [162]. CTCs usually present a dormant state [162] where CTC is relatively stiffer. When they become malignant ones, the stiffness decreases significantly [163]. Many literature reported that the Young's modulus for cancer cells. Those data are measured using atomic force microscopy(AFM). The cell bending stiffness for white blood cells is about $2 \times 10^{-18} J$ in temperature of $300^{\circ} K$ [164].Thus, two bending stiffness of 2×10^{-16} and $2 \times 10^{-18} kg.m^2.s^{-2}$ are chosen to represent stiff and soft particles, respectively. Moreover, to cover a range of size and shape variations, $8\mu m$ RBC and $4\mu m$, $8\mu m$ and $12\mu m$ circular particles are used in the simulation, as shown in Figure 5.1. It is observed that the flow field disturbance caused by effective and recovery strokes of ciliary array efficiently repel away particles as shown in Figure 5.2. Additionally, high velocity gradient close to upper wall also prevent particles to get close to upper boundary. Their dynamics is similar to cell-free layer in microcirculatory vessels where red blood cells move away from vessel wall[165]. Also, the disturbance created by synchronized motion of cilia enhance this effect. Thus, all particles regardless of size, shape, stiffness or the position they are initially released from, tend to gradually move to the center of channel as shown in Figure 5.2. However, their transition speed are different and depend on their physical property.

It is hypothesized that we might be able to utilize the effect of size, shape and stiffness on transition speed to stabilize particles at different heights of the 2D channel. Thus, to differentiate particles, a small uniform flow, $\overline{U}_z/\overline{U}_x = 0.004$, from lower to upper wall perpendicular to the main flow is introduced. It is observed that microparticles will flow downstream at different heights of microchannel as shown in Figure 5.3. Also, smaller particles move closer to upper wall due to their lower transition speed as described in

Figure 5.2. However, bigger particle are less influenced by lateral flow because coordinate motion of cilia more effectively draw them to the channel center. Similarly, the slight difference between the motion of soft and stiff particles, with same size and shape, can be attributed to their distinct transition speeds as shown in Figure 5.2. In other word, stiffer particles respond more quickly to every stroke of cilia which result in moving marginally above their softer counterpart as shown in Figure 5.3. Overall, although separation distance between particle's trajectories in Z direction are insignificant in 2D, it shows that difference in physical property can result in some degree of separation. Using 2D simulation, we initially tried to describe why particles tend to move to the center of channel. And for the part where the lateral flow is introduced, the possibility of particle separation is primarily demonstrated. After explaining the dynamics of particle-cilia interaction in 2D, we know move on to 3D setup where the flow dynamic gets more complex.

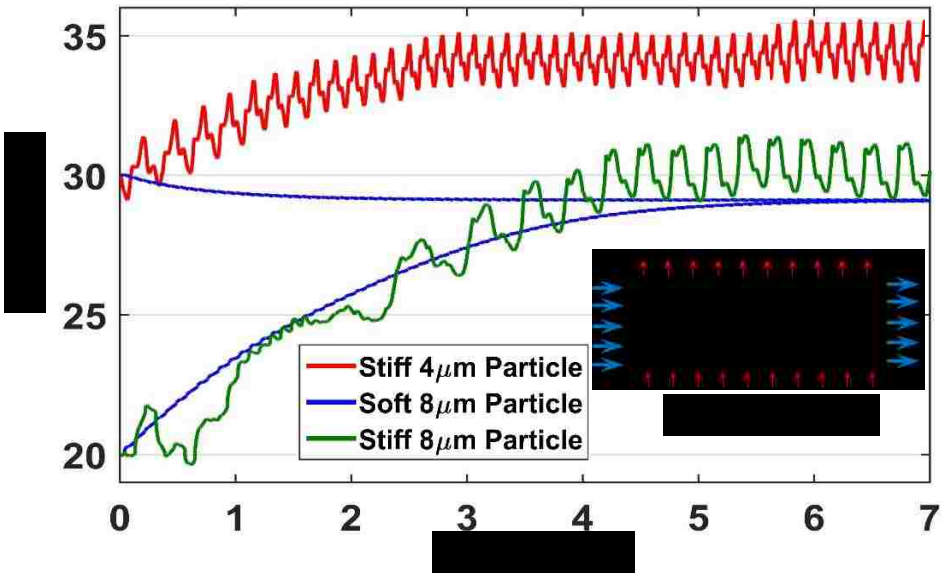

Figure 5.3. Due to cross-flow, particles stabilize in different streamlines depending on their biophysical properties. The solid blue lines represent the trajectories of soft 8 μm particles initially released from different heights.

5.2 3D model

It is shown that biophysical properties of flow particles directly influence the dynamics of their interaction with ciliary system. By generating a lateral drifting force, we aim to use this unique feature to separate/sort flow particles along the width of the channel. Particles can move laterally when cilia array are placed with an angle to the main flow similar to Herringbone structures[166]. Cilia spacing along channel length is assumed $25\mu m$ where rows are tilted 30˚ as shown in Figure 5.4. Due to significantly higher computational cost of 3D model, the respective dimensions of simulation box are $L_x \times L_y \times L_z = 50 \times 50 \times 80$ LB units where periodic boundary condition are applied in X directions. In both upper and lower walls, Zou/He bounce back rules[167] is used to enforce non-slip wall boundary condition. Since the width of real channel is many times larger, periodic boundary condition is used in Y directions. Similar to 2D model, $4, 8, 12\mu m$ spherical particles and $8\mu m$ RBC are chosen to study separation dynamics of particles with different sizes and shapes as shown in Figure 5.4.

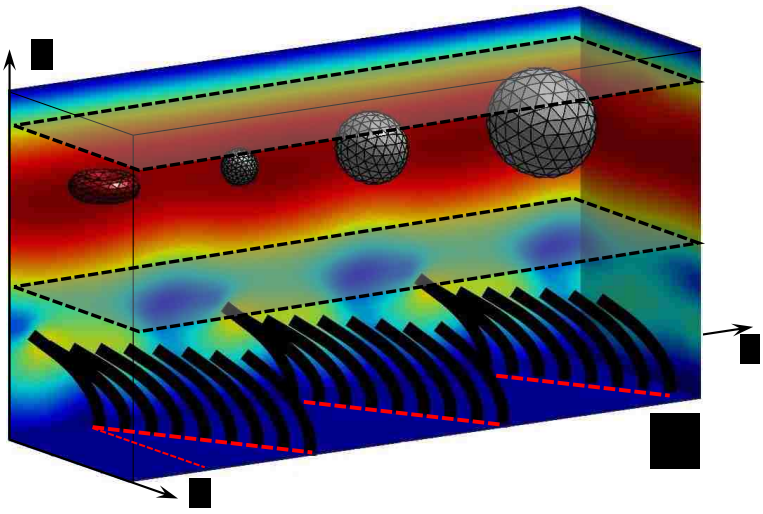

Figure 5.4. 3D demonstration of particle-cilia interaction in microchannel.

Various bending stiffness have been suggested for WBC and RBC in literature [62, 127, 164]. To cover the target range of bending stiffness for both healthy and unhealthy blood cells as well as CTC, two bending stiffness of 5×10^{-17} and $5 \times 10^{-19} kg.m^2.s^{-2}$ are chosen to represent soft and stiff particles in 3D. Other model parameters are chosen so that $L_z = 40\mu m$, $N_{cilium} = 26$, $r_{cilium}/l = 0.016$, $L_z/l = 3$, $Re = 0.2$, $\mathrm{Sp} = 6$, $F_{x0}l^2/EI = 64$ and $F_{z0}/F_{x0} = 4$. It should be noted that 320 triangular elements are used to mesh particle's membrane and the local area constraint, global area constraint and volume constraint constants are chosen as $23.1 \times 10^{-5}\ kg.s^{-2}$, $4.72 \times 10^{-6}\ kg.s^{-2}$ and $249\ kg.m^{-1}.s^{-2}$, respectively. To eliminate any residue membrane stress at equilibrium state, nodes are allowed to move on the membrane to minimize in-plane energy before starting the simulation. In this stress free condition, the membrane is relaxed and equilibrium lengths of springs are recalculated. More detail information about spring network model can be found in [62].

In 2D, it was observed that all particles are effectively repelled away by harmonic motion of cilia. It is also shown that flow in Z direction can differentiate particle. Similarly in 3D, the position of particles along Z axis are stabilized at different height of channel even though they are released from same location as shown in Figure 5.5. Because cilia array is positioned in an angle respect to main flow, it creates a fluid motion in Z direction and similar to cross flow case in 2D which leads to particle separation 4mm downstream.

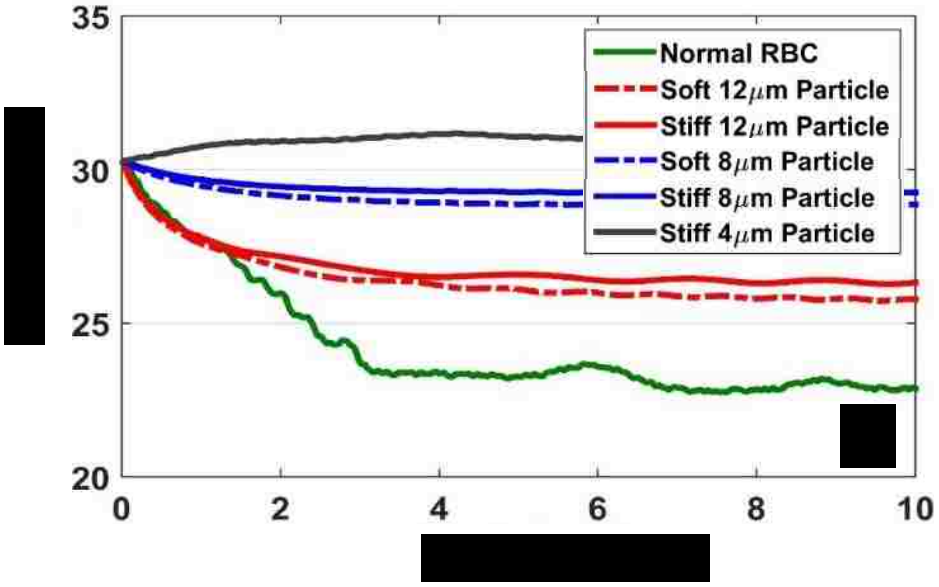

Figure 5.5. Particles with distinct biophysical properties tend to flow downstream in different height of microchannel.

Harmonic motion of tilted cilia array also laterally displaces particles in Y direction as demonstrated in Figure 5.6 and Supplementary Movie 1. However, the magnitude of lateral drifting velocity is considerably smaller than the main flow. To provide a better insight into underlying physics, the streamlines during one actuation cycle are demonstrated in Supplementary Movie 2. It is observed that $12\mu m$ particles tend to laterally drift more compared to $8\mu m$ and $4\mu m$ particles. Also, the $8\mu m$ RBC is shown to displace even more than $12\mu m$ spherical particles by 10% because of its biconcave shape. The lateral drifting velocity also depend on the membrane bending stiffness. Similar to 2D cases, softer particle tend to move closer to cilia along Z axis. This slight difference in height can effectively influence their lateral motion.

It is demonstrated in Figure 5.6 that the stiff $12\mu m$ particles drift 6% more compared to their softer counterpart with same biophysical properties. Furthermore, to check if the sorting process is not based on the main flow, a case with 12μm particles in a channel with unactuated ciliary system is also simulated as shown in Figure 5.6. Similar to Herringbone structures, unactuated tilted ciliary system also can laterally displace particles but cannot effectively separate particles. It is observed that separation efficiency of soft and stiff particles in unactuated system is 10 times smaller than actuated ciliary system. The separation efficiency can be defined as the ratio of the separation distance between two trajectories to the length particles move downstream, $S_e = \Delta z/\Delta x$. Overall, using this setup, target particles with specific biophysical property can be isolated from a heterogeneous population because they follow a unique lateral trajectories as shown in Supplementary Movie 3. The dynamics of interaction between cilia and microparticles can be better realized by watching three multimedia files provided under electronic supplementary information.

To check if the sorting process is not based on main flow and passive presence of cilia, a case with 12μm particles in a channel with unactuated ciliary system is also simulated as shown in Figure 5.6. Similar to Herringbone structures, unactuated tilted ciliary system can also laterally displace particles but cannot effectively separate particles. It is observed that separation efficiency of soft and stiff particles in unactuated system is 10 times smaller than actuated ciliary system. The separation efficiency can be defined as the ratio of the separation distance between two trajectories to the length particles move downstream, $S_e = \Delta z/\Delta x$. Overall, using this setup, target particles with specific biophysical property can be isolated from a heterogeneous population because they follow a unique lateral trajectories

as shown in Supplementary Movie 3. The dynamics of interaction between cilia and microparticles can be better realized by watching three multimedia files provided as electronic supplementary information.

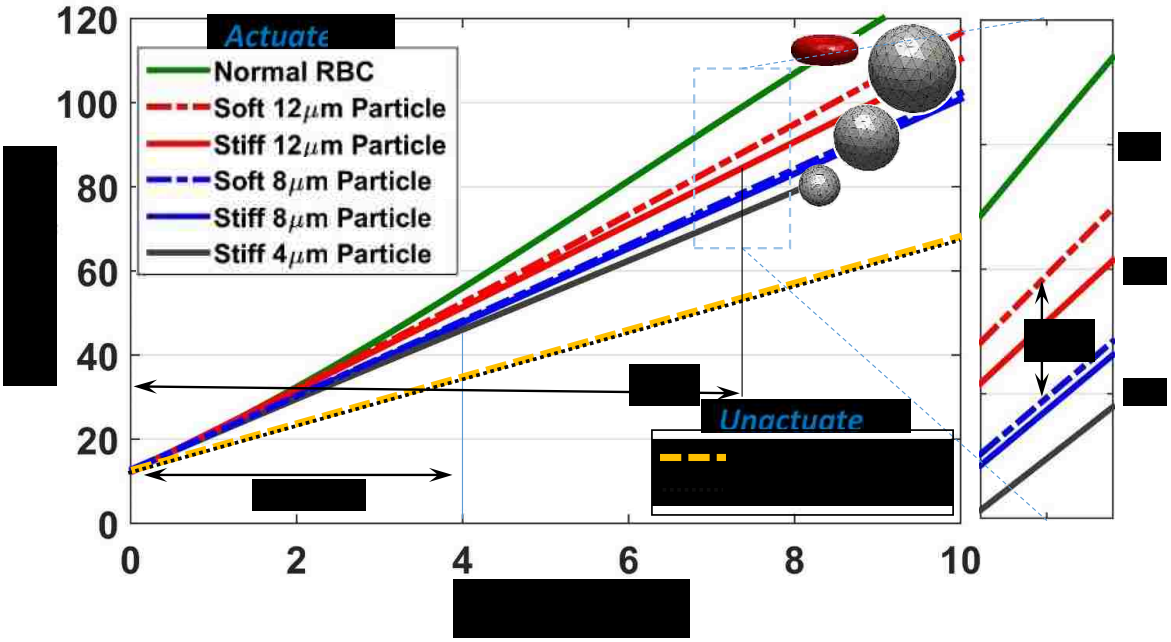

Figure 5.6. Size, shape and stiffness dependent trajectories of particles due to harmonic motion of tilted cilia array. As particles flow downstream in the X direction, they also displace laterally in the Y direction. After transition period, particle's position in Z direction do not change anymore. The yellow dashed and dotted black lines represent the case with soft and stiff 12μm particle where cilia is not actuated. Separation efficiency is defined as the ratio of the separation distance between two trajectories to the length particles move downstream, $\boldsymbol{S_e = \Delta z/\Delta x}$.

5.3 Parameter study

It is worthy to mention that the cilia-particle interaction can be significantly affected by actuation frequency, cilia array angle, and cilia length. In this dissertation, we initially study influence of cilia array angle on particle's lateral velocity. Later, it will be shown that this model parameter can be tuned based on our preference. Cilia array with 20˚, 30˚, 45˚ and 60˚ angles are simulated to investigate the effect of this parameter on separation

dynamics, see Figure 5.7. In the case where active cilia arrays are placed in 45˚ angle, it is observed that larger lateral displacement can be achieved. Additionally, 30˚ angle ciliary array is shown to have higher separation efficiency when it is separating particle based on their bending stiffness. On the contrary, trajectories of particles with different sizes are more effectively distanced when cilia array angle is 45˚.

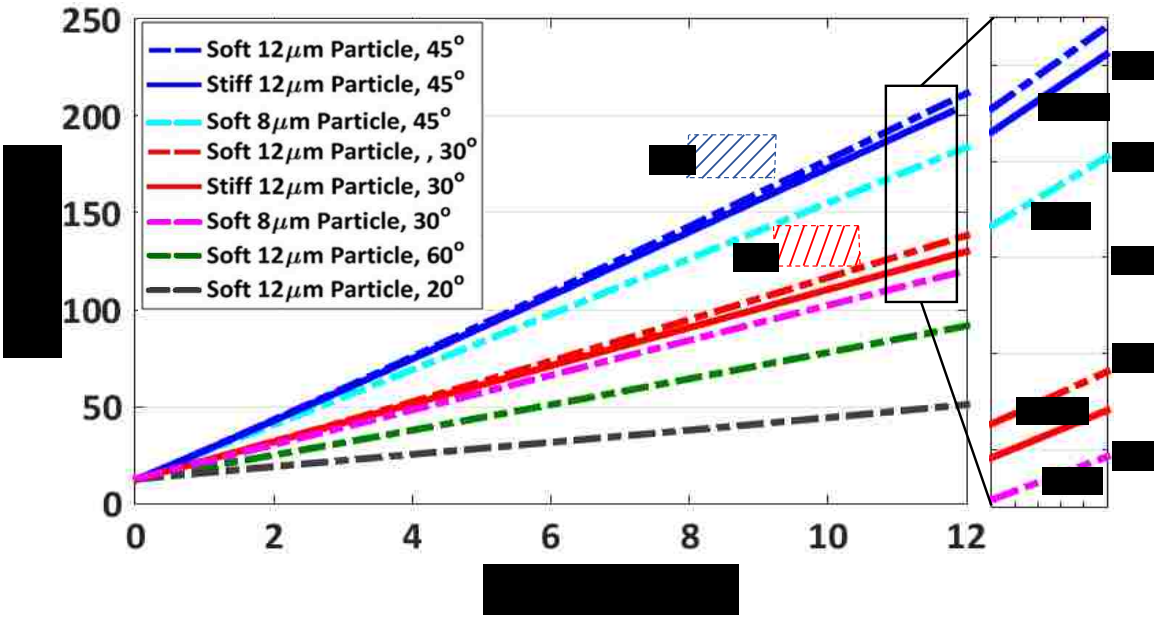

Figure 5.7. The effect of ciliary angle on lateral displacements and separation efficiencies of soft particulates.

Also, actuation mode of external magnetic field directly can be translated into beating frequency of active ciliary system. This model parameter can also significantly influence the displacement of flow particles along Y axis as shown in Figure 5.8. It can be seen that in high beating frequencies, the lateral displacement is generally larger. Moreover, it is illustrated in Figure 5.8 that in 120Hz, stiffness based separation efficiency of $12\mu m$ is largest.

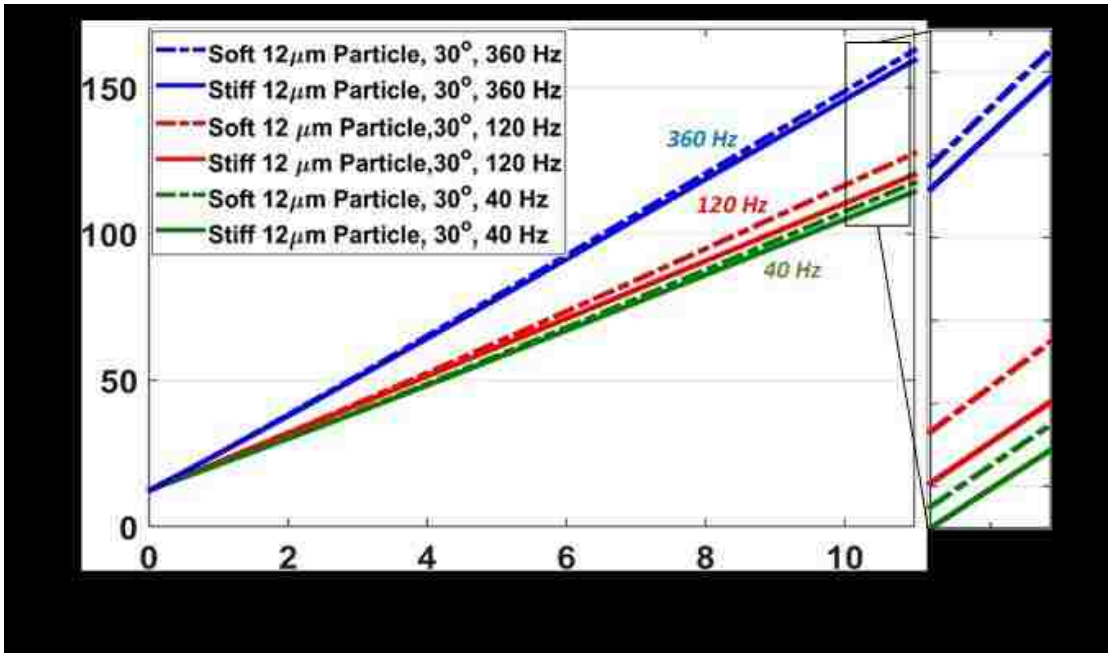

Figure 5.8. The effect of actuation frequency on lateral displacement of soft and stiff 12μm particles.

The dimension of cilia with respect to channel height is also important in cilia-particle interaction. Thus, we have performed simulation for cases with different cilia to channel height ratios. It is shown in Figure 5.9 that the ciliary system with higher aspect ratio generate larger lateral force on flow particulates. Similar to previous model parameter, the lateral displacement flow particles will be different when cilia height increase or decrease as we keep channel height constant. Accordingly size, shape and stiffness based separation efficiency will also be affected. As shown in Figure 5.9, the size based separation efficiency is 8.6% for cilia array with 0.33 aspect ratio while it is 6.5% for 0.4 aspect ratio. However, the ciliary system with 0.4 aspect ratio is found to be more capable of separating particles based on their bending stiffness.

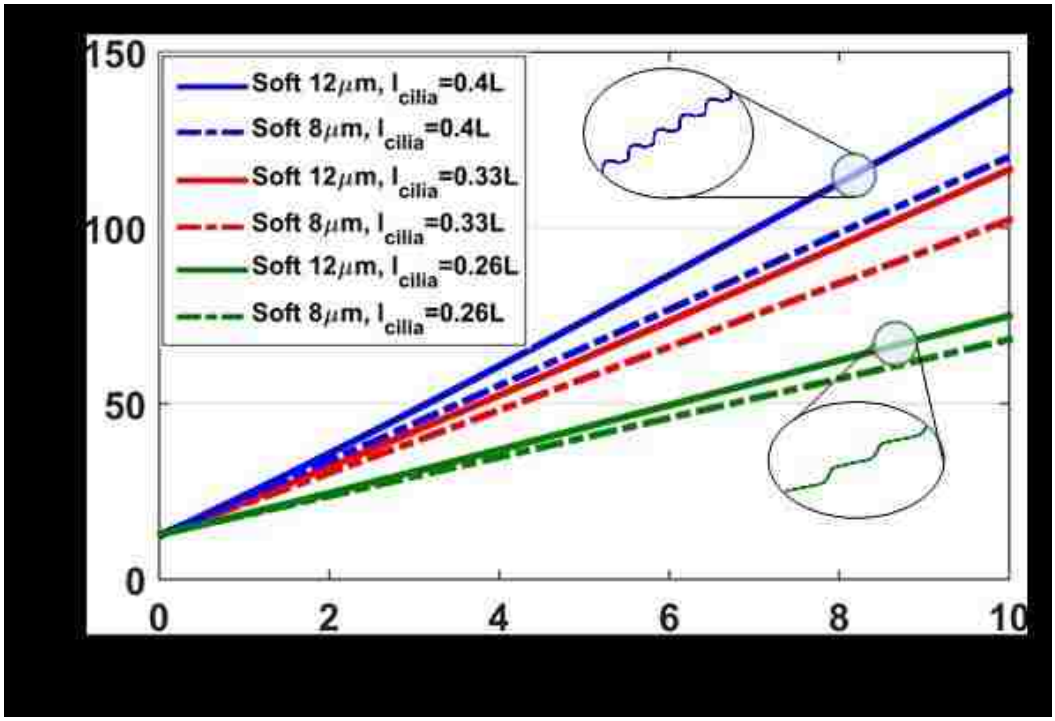

Figure 5.9. The effect of ciliary aspect ratio on lateral displacement and separation efficiency of soft 8μm and 12μm particles. The zoom-in images demonstrate the oscillations in particle's trajectory because of synchronized motion of cilia.

5.4 Separation device design

In the previous section, it is extensively discussed that soft microparticles follow specific streak lines based on their unique biophysical properties when flowing in a microfluidic channel covered with active artificial cilia. Here, we will utilize our previous findings to propose a design for of an active ciliary system which can separate particle based on biophysical properties with high efficiency. As mentioned before, the separation efficiency based on shape, size and stiffness strongly depend on cilia array angle. This unique characteristic can be used to design an efficient ciliary pattern to separate subpopulation of particles from a heterogeneous mixture.

It was shown that ciliary system with 0.33 length ratio, 30˚ ciliary angle, and $120Hz$ actuation frequency can laterally move microparticle by $\sim 100\mu m$ in $10mm$ length of the channel. Readers can refer to Figure 5.6. Moreover, it is observed that particle's trajectories are separated by 2% to 15%. This percentage can be translated to 2 to $15\mu m$ gap between their mass centres at the outlet of channel. To gain more separation, we need to utilize wider channel. Physically, we definitely have limitation on the width of microfluidic device and we cannot make it unrealistically large. To solve this problem, we can use ciliary arrays in blocks with different angles. The reason for doing this will be explained shortly. It can be simply concluded that by placing a $0.5mm$ block with 45˚ cilia angle after $1mm$ block with 30 ˚ cilia angle, particles can be re-directed in opposite direction to their original position. However, we can use this specific characteristics of active ciliary system where the separation efficiencies varies for patterns with different ciliary angles. It should be noted that we can do repeat this process multiple times. In Figure 5.10, we demonstrate the schematics of the proposed idea. Moreover, we have also added an expansion nozzle where we can further increase separation gap between particles with various biophysical properties. One interesting feature of this design is that we can even detect a slight difference in stiffness of suspended soft particles. Specifically for CTCs where the isolation is hard and their stiffness is slightly different from normal healthy cells [163]. Based on separation efficiency as low as 0.1% between two subpopulation of microparticles, it is shown that they can be distanced by $200\mu m$ at the end of expansion nozzle in a 20cm microfluidic channel. Therefore, using our proposed design, we can isolate target particles in just one step with high throughput as shown in Figure 5.10. Assuming 15mm/s average

velocity fluid in microfluidic device and 50μm distance between two consecutive particles, we estimate that we can separate 300 particles per second using this approach.

In our proposed design, one pattern can be used for different isolation of different target particles. As mentioned in previous sections, beating frequency also influence lateral displacement of particle with different size, shape and stiffness. Readers can refer to Figure 5.10 for more information. Therefore, just by tuning actuation frequency we can completely slightly change the separation dynamics and change it to our desirable scheme. It is noteworthy to mention that the scope of this dissertation along this idea was focused on the conceptual design and numerical simulation of ciliary system. The potential future work along this work will be discussed in the following.

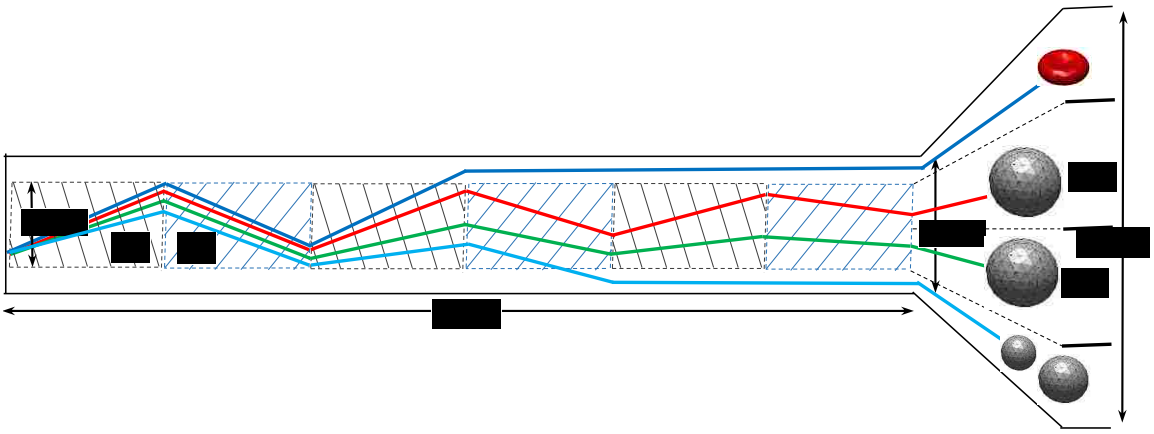

Figure 5.10. The schematics of a high-throughput, optimized particle sorter for efficient isolation of target particles with specific biophysical property.

Chapter 6: Conclusion

6.1 Shear induced cell damage

Prolonged contact and collision between blood cells and device surfaces and regions of high shear stress contribute to cell damage [18, 19]. Under high shear rates, pores form on RBC membrane through which hemoglobin leaks out and increases free hemoglobin content of plasma leading to hemolysis. In this dissertation, a novel model is presented to study red blood cell (RBC) hemolysis at cellular level which can directly correlate the microscale state of the cell membrane to local stress/strain distribution and correspondingly hemoglobin release. Our approach is comprised of three sub-models: defining criteria of pore formation, calculating pore size, and measuring Hb diffusive flux out of pores. Our damage model uses information of different scales to predict cellular level hemolysis. Results are compared with experimental studies and other models in literature. The developed cellular damage model can be used as a predictive tool for hydrodynamic and hematologic design optimization of blood-wetting medical devices.

To simulate deformation of RBC, spring connected model of erythrocyte membrane is coupled with lattice Boltzmann through immersed boundary method. RBC stretching and shearing tests are performed to validate our cell model. The dynamics of cell rupture is studied when spectrin network is damaged under high stretching forces. Moreover, the local conditions which leads to initiation of pore formation and sublytic damage of RBC are also studied. It is found that pores continuously appear/disappear as RBC tank-treads under high shear flows. After identifying the size and location of these nanopores, Hb flux is measured to calculated index of hemolysis in term of exposure time. Finally, it is shown that hemolysis predicted from our cellular model results agrees well with experimental studies.

As noted before, experimental evaluation of damage strongly depends on test device and experiment condition. Thus, we have linked cellular level damage to hemoglobin release to address this issue. Using this method, we are able to develop a general criteria independent of particular device. Furthermore, unlike previous approaches we studied hemolysis locally by obtaining model parameters from underlying molecular dynamic simulations. Overall, our novel cellular approach can be used as a predictive tool to microscopically evaluate flow induced damage in any general device.

6.2 Soft particle sorting by ciliary system

Simple and efficient particle separation methods are fundamentally important in biological and chemical analyses such as cancer cell detection, rare cell isolation, tissue engineering, and drug screening. In this dissertation, a novel approach is proposed to isolate a specific

subpopulations of microparticles using active ciliary system. Our model utilizes immersed boundary (IB) method coupled with lattice Boltzmann. Soft particle and cilia are implemented through spring connected network model and point-particle scheme, respectively. It should be noted that unlike previous studies, we do not assume adhesive interaction between the particles and cilia. Therefore, antifouling characteristics of cilia array prevent any direct contact between cilia and sensitive particulates.

3D simulations are carried out to closely study cilia-particle interaction and isolation dynamic. It is observed that soft microparticles flow downstream in different trajectories based on their biophysical properties. It is hypothesized that depending on their closeness to beating cilia, they will experience different lateral forces. Through 3D simulations, we showed how particles with different physical properties move at different heights above ciliated wall. Because of that, soft microparticles may follow different lateral trajectories and therefore can be sorted along the width of the channel. The goal of this modeling effort was to demonstrate that our approach is capable of continuously and non-destructively separating cells into subpopulations based on their size, shape and stiffness with high throughput. At the end, proper structural parameters for an active ciliary system capable of isolating microparticles with high separation efficiency is provided. We have shown that our design is very sensitive to changes in stiffness. Overall, it is shown that our programmable/high throughput microfluidic device is biocompatible which can greatly complement existing separation technologies.

6.3 Future work

The future work section includes two part. The first part, is to explore the potential works that can be done on RBC hemolysis in future. In the second part, we discuss how we can actually fabricate microfluidic device which is capable of separating particles.

6.3.1 Potential future work on RBC hemolysis

Our multiscale damage model can be significantly improved by studying each submodels separately in more depth. For instance, hindered diffusion coefficient of Hb molecules out of small pores in lipid bilayer can be accurately estimated by CGMD simulations. Furthermore, it should be mentioned that our approach can only handle mechanical damages. The damages to RBC membrane by chemical changes such as iron deficiency which influences lifespan of RBCs in circumstance like acidemia and oxidative stress [168] are not considered in this dissertation but can be implemented as input to our model in the future. For instance, we can input chemical damages by modifying bending stiffness and area constraint constants of RBC membrane. In this situation, by altering the physical property of the RBCs, one can observe that the characteristics of RBC itself may affect hemolysis.

In addition to these limitations, it should be mentioned that our damage model focuses on Hb diffusion out of a single RBC compared to macroscale estimation of hemolysis in typical experimental setups. RBCs in actual biomedical devices take different pathways and undergo various stress history. To make full use of our single cell damage model, we also need to establish complementary computational techniques to predict hemolysis in complex flow conditions, i.e., blood-wetting biomedical devices. Because of high

computational costs of our numerical model, we are limited to use a statistical sampling approach to evaluate damage in a big computational domain. Therefore, we can only apply our model to a handful of sample RBCs in the flow to assess damage in an actual biomedical device. Moreover, in conjunction with experimental validation using microfluidic system, this integrated modeling can help elucidate the dynamics of blood cell in complex flow environment and serves as a blood cell damage evaluation tool.

It was mentioned that for future work on this topic, we need to drastically increase the speed of our computations. To address this issue, we can exploit one of the promising features of LBM which is its capabilities of taking advantage of parallel computing. The local streaming and collision nature enables us to run the fluid solver based on geometric decomposition. There are two popular open source codes such Sailfish [169], and Palabos [170] which use graphic processing units (GPU) and message passing interface (MPI) for parallelization, respectively. By using coupling these well-written codes and our multiscale damage model, we study single cell hemolysis in real biomedical device.

Besides medical devices and red blood cell damage, cell damage is also a very important concern in devices such as syringe pump [171], and bio-printer [172]. In these devices, the dynamic of cell deformation and damage may be different from shear-induced hemolysis of RBC. For instance, in biofabrication and microfluidic lab on-chip devices [173], individual or groups of cells are manipulated in a small channel such as syringe-based cell deposition for tissue constructs [174] and inkjet-based cell printing [175]. Thus, looking into these type of damage which considerably may reduce cell viability can be a very good topic for future study on this topic.

6.3.2 Cilia fabrication and actuation

Various methods have been proposed for fabrication of magnetic cilia [176-183]. The diameter and height of cilia widely varies based on the approach utilized for fabrication. The other important feature is that microfluidic device should be fabricated in a way that cilia embedded in a closed micro channel. One method of fabrication is that PCTE porous membrane can be used as mold. After curing PDMS-magnetic particle mixture in the mold, PCTE membrane can be dissolved [181]. By this approach, we can only achieve very high aspect ratio and nanoscale cilia and there cannot have the desirable pattern since cilia are placed randomly on substrate. In another approach, we can use acrylic blocks and drill holes in them by micromachining tools [180]. After curing PDMS-magnetic particle mixture inside the holes, we can simply dissolve acrylic with Acetone. However, drilling process is very tedious and time consuming. Furthermore, the mold is only one time use. Silicon wafers can also be prepared by photolithography method[179] and utilized to fabricate magnetically-actuated cilia. However, one cannot achieve high aspect ratio since the peeling PDMS from wafer is very difficult and cilia can break during this process. Candy-base replica[182] can also be used for cilia fabrication. However, it will need a primary mold and working with sugar-based mold can be very difficult. Alternatively, cilia in microfluidic channel can be fabricated in one step using micro stereolithography methods [139, 184, 185]. But, 3D printing small features with high resolution is still challenging with this technology. Thus, it can be concluded that the fabrication of cilia inside micro-channels seems practical. As the step of conceptual design, we can move in the direction of cilia fabrication and test our isolation idea in real microfluidic setup.

REFERENCE

1. Yunus, D.E., et al., *Shear induced alignment of short nanofibers in 3D printed polymer composites.* Nanotechnology, 2016. **27**(49): p. 495302.

2. Yunus, D.E., et al., *Short fiber reinforced 3d printed ceramic composite with shear induced alignment.* Ceramics International, 2017.

3. Sohrabi, S., et al., *Characterization of nanoparticle binding dynamics in microcirculation using an adhesion probability function.* Microvascular Research, 2016. **108**: p. 41-47.

4. Sohrabi, S., et al., *Nanoparticle transport and delivery in a heterogeneous pulmonary vasculature.* Journal of Biomechanics, 2017. **50**: p. 240-247.

5. Tan, J., et al., *Characterization of Nanoparticle Dispersion in Red Blood Cell Suspension by the Lattice Boltzmann-Immersed Boundary Method.* Nanomaterials, 2016. **6**(2): p. 30.

6. Liu, Y., et al., *The configuration of copolymer ligands on nanoparticles affects adhesion and uptake.* Langmuir, 2016. **32**(39): p. 10136-10143.

7. Liu, Y., et al., *Antibody-coated nanoparticles are promising molecular probes for microscopic analysis of cell behavior*. 2016, Future Medicine.

8. Zhou, Y., et al., *Mechanical Properties of Nanoworm Assembled by DNA and Nanoparticle Conjugates.* Journal of Nanoscience and Nanotechnology, 2016. **16**(6): p. 5447-5456.

9. Hoogerbrugge, P. and J. Koelman, *Simulating microscopic hydrodynamic phenomena with dissipative particle dynamics.* EPL (Europhysics Letters), 1992. **19**(3): p. 155.

10. O'connell, S.T. and P.A. Thompson, *Molecular dynamics–continuum hybrid computations: a tool for studying complex fluid flows.* Physical Review E, 1995. **52**(6): p. R5792.

11. Fyta, M., et al., *Coupling Lattice Boltzmann with atomistic dynamics for the multiscale simulation of nano-biological flows.* arXiv preprint arXiv:0710.1272, 2007.

12. Tan, J., *Lattice Boltzmann Method and Its Applications in Soft Matter*. 2015: Lehigh University.

13. Throckmorton, A.L., et al., *Numerical, hydraulic, and hemolytic evaluation of an intravascular axial flow blood pump to mechanically support Fontan patients.* Annals of biomedical engineering, 2011. **39**(1): p. 324-336.

14. Castellini, P., M. Pinotti, and L. Scalise, *Particle image velocimetry for flow analysis in longitudinal planes across a mechanical artificial heart valve.* Artificial organs, 2004. **28**(5): p. 507-513.

15. Shi, W., R. He, and Y. Liu, *3D printing scaffolds with hydrogel materials for biomedical applications.* European Journal of BioMedical Research, 2015. **1**(3): p. 3-8.

16. Ku, D.N., *Blood flow in arteries.* Annual Review of Fluid Mechanics, 1997. **29**(1): p. 399-434.

17. Tillmann, W., et al., *In-vitro wall shear measurements at aortic valve prostheses.* Journal of biomechanics, 1984. **17**(4): p. 263-279.

18. Kormos, R., et al., *Rheologic abnormalities in patients with the Jarvik-7 total artificial heart.* ASAIO Journal, 1987. **33**(3): p. 413-417.

19. Hung, T.-C., et al., *Effects of long-term Novacor artificial heart support on blood rheology.* ASAIO transactions/American Society for Artificial Internal Organs, 1990. **37**(3): p. M312-3.

20. Vural, K.M., *Ventricular assist device applications.* Anadolu Kardiyoloji Dergisi-the Anatolian Journal Of Cardiology, 2008. **8**: p. 117-130.

21. Mccarthy, P.M., *Heartmate Implantable Left-Ventricular Assist Device - Bridge To Transplantation And Future Applications.* Annals Of Thoracic Surgery, 1995. **59**(2): p. S46-S51.

22. AlJarallah, A.S., et al., *The Hemopump as a left ventricular assist device in pediatric applications: Initial Canadian applications.* Canadian Journal Of Cardiology, 1997. **13**(5): p. 489-494.

23. Polaschegg, H.-D., *Red Blood Cell Damage from Extracorporeal Circulation in Hemodialysis.* Seminars in Dialysis, 2009. **22**(5): p. 524-531.

24. Polaschegg, H.D. *Red blood cell damage from extracorporeal circulation in hemodialysis*. in *Seminars in dialysis*. 2009. Wiley Online Library.

25. Canham, P.B. and D.R. Parkinson, *The area and volume of single human erythrocytes during gradual osmotic swelling to hemolysis.* Canadian journal of physiology and pharmacology, 1970. **48**(6): p. 369-376.

26. Kinosita, K. and T. Tsong, *Hemolysis of human erythrocytes by transient electric field.* Proceedings of the National Academy of Sciences, 1977. **74**(5): p. 1923-1927.

27. Tsong, T.Y. and E. Kingsley, *Hemolysis of human erythrocyte induced by a rapid temperature jump.* Journal of Biological Chemistry, 1975. **250**(2): p. 786-789.

28. Chien, S., S.A. Luse, and C.A. Bryant, *Hemolysis during filtration through micropores: A scanning electron microscopic and hemorheologic correlation.* Microvascular research, 1971. **3**(2): p. 183-203.

29. Sutera, S. and M. Mehrjardi, *Deformation and fragmentation of human red blood cells in turbulent shear flow.* Biophysical journal, 1975. **15**(1): p. 1.

30. Ohta, Y., et al., *Atomic force microscopic observation of mechanically traumatized erythrocytes.* Artificial organs, 2002. **26**(1): p. 10-17.

31. Grimm, J., et al., *Hemolytic effect of deformed intra-arterial stents and stent grafts in vitro.* European Radiology, 2003. **13**(6): p. 1333-1338.

32. Xu, J., et al., *Finite Element Analysis of the Implantation Process of Overlapping Stents.* Journal of Medical Devices, 2017. **11**(2): p. 021010.

33. Blackshear, P. and G. Blackshear, *Mechanical hemolysis.* Handbook of Bioengineering. New York: McGraw-Hill, 1987. **15**: p. 1-9.

34. Gefen, A., et al., *Strain-time cell-death threshold for skeletal muscle in a tissue-engineered model system for deep tissue injury.* Journal of Biomechanics, 2008. **41**(9): p. 2003-2012.

35. Steinhardt, R.A., G.Q. Bi, and J.M. Alderton, *Cell-Membrane Resealing by a Vesicular Mechanism Similar to Neurotransmitter Release.* Science, 1994. **263**(5145): p. 390-393.

36. Cui, X.F., et al., *Cell Damage Evaluation of Thermal Inkjet Printed Chinese Hamster Ovary Cells.* Biotechnology and Bioengineering, 2010. **106**(6): p. 963-969.

37. Wood, H.G., et al., *The medical physics of ventricular assist devices.* Reports on Progress in Physics, 2005. **68**(3): p. 545.

38. Behbahani, M., et al. *Towards shape optimization for ventricular assist devices using parallel stabilized FEM*. in *Proceedings of the NIC Symposium*. 2008.

39. Wu, J., et al., *Numerical investigation of the effects of channel geometry on platelet activation and blood damage.* Annals of Biomedical Engineering, 2011. **39**(2): p. 897-910.

40. Song, X., et al., *Quantitative evaluation of blood damage in a centrifugal VAD by computational fluid dynamics.* Journal of fluids engineering, 2004. **126**(3): p. 410-418.

41. Rother, R.P., et al., *The clinical sequelae of intravascular hemolysis and extracellular plasma hemoglobin: A novel mechanism of human disease.* JAMA, 2005. **293**(13): p. 1653-1662.

42. Stewart, S.F., et al., *Results of FDA's First Interlaboratory Computational Study of a Nozzle with a Sudden Contraction and Conical Diffuser.* Cardiovascular Engineering and Technology, 2013. **4**(4): p. 374-391.

43. Stewart, S.F., et al., *Preliminary results of FDA's 'Critical Path'project to validate computational fluid dynamic methods used in medical device evaluation.* ASAIO J, 2009. **55**(2): p. 173.

44. Stewart, S.F., et al., *Assessment of CFD performance in simulations of an idealized medical device: results of FDA's first computational interlaboratory study.* Cardiovascular Engineering and Technology, 2012. **3**(2): p. 139-160.

45. Hariharan, P., et al., *Multilaboratory particle image velocimetry analysis of the FDA benchmark nozzle model to support validation of computational fluid dynamics simulations.* Journal of biomechanical engineering, 2011. **133**(4): p. 041002.

46. Giersiepen, M., et al., *Estimation of shear stress-related blood damage in heart valve prostheses--in vitro comparison of 25 aortic valves.* The International journal of artificial organs, 1990. **13**(5): p. 300-306.

47. Zhang, T., et al., *Study of Flow ‐ Induced Hemolysis Using Novel Couette ‐ Type Blood ‐ Shearing Devices.* Artificial organs, 2011. **35**(12): p. 1180-1186.

48. Bludszuweit, C., *Model for a general mechanical blood damage prediction.* Artificial organs, 1995. **19**(7): p. 583-589.

49. Yeleswarapu, K.K., et al., *A Mathematical Model for Shear ‐ Induced Hemolysis.* Artificial organs, 1995. **19**(7): p. 576-582.

50. Okamoto, E., et al., *Blood Compatible Design of a Pulsatile Blood Pump Using Computational Fluid Dynamics and Computer ‐ Aided Design and Manufacturing Technology.* Artificial organs, 2003. **27**(1): p. 61-67.

51. Arora, D., M. Behr, and M. Pasquali, *Blood damage measures for ventricular assist device modeling.* Artificial Organs, accepted (April 2004), 2003.

52. Arora, D., M. Behr, and M. Pasquali, *A Tensor ‐ based Measure for Estimating Blood Damage.* Artificial Organs, 2004. **28**(11): p. 1002-1015.

53. Yan, K.C., K. Nair, and W. Sun, *Three dimensional multi-scale modelling and analysis of cell damage in cell-encapsulated alginate constructs.* Journal of Biomechanics, 2010. **43**(6): p. 1031-1038.

54. Chen, Y. and M.K. Sharp, *A Strain‐Based Flow‐Induced Hemolysis Prediction Model Calibrated by In Vitro Erythrocyte Deformation Measurements.* Artificial organs, 2011. **35**(2): p. 145-156.

55. Ezzeldin, H.M., et al., *A Strain-Based Model for Mechanical Hemolysis Based on a Coarse-Grained Red Blood Cell Model.* Annals of biomedical engineering, 2015: p. 1-12.

56. Vitale, F., et al., *A multiscale, biophysical model of flow-induced red blood cell damage.* AIChE Journal, 2014: p. n/a-n/a.

57. Koshiyama, K. and S. Wada, *Molecular dynamics simulations of pore formation dynamics during the rupture process of a phospholipid bilayer caused by high-speed equibiaxial stretching.* Journal of biomechanics, 2011. **44**(11): p. 2053-2058.

58. Groot, R.D. and K.L. Rabone, *Mesoscopic simulation of cell membrane damage, morphology change and rupture by nonionic surfactants.* Biophysical Journal, 2001. **81**(2): p. 725-736.

59. Neder, J., et al., *Coarse-grained simulations of membranes under tension.* Journal of Chemical Physics, 2010. **132**(11).

60. Li, J., et al., *Cytoskeletal dynamics of human erythrocyte.* Proceedings of the National Academy of Sciences, 2007. **104**(12): p. 4937-4942.

61. Vitale, F., et al., *A multiscale, biophysical model of flow‐induced red blood cell damage.* AIChE Journal, 2014. **60**(4): p. 1509-1516.

62. Fedosov, D.A., B. Caswell, and G.E. Karniadakis, *A multiscale red blood cell model with accurate mechanics, rheology, and dynamics.* Biophysical journal, 2010. **98**(10): p. 2215-2225.

63. Liu, Y. and W.K. Liu, *Rheology of red blood cell aggregation by computer simulation.* Journal of Computational Physics, 2006. **220**(1): p. 139-154.

64. Liu, W.K., et al., *Immersed finite element method and its applications to biological systems.* Computer Methods in Applied Mechanics and Engineering, 2006. **195**(13-16): p. 1722-1749.

65. Tan, J., A. Thomas, and Y. Liu, *Influence of red blood cells on nanoparticle targeted delivery in microcirculation.* Soft Matter, 2012. **8**(6).

66. Tan, J., et al., *The influence of size, shape and vessel geometry on nanoparticle distribution.* Microfluidics and Nanofluidics, 2013. **14**(1-2): p. 77-87.

67. Tan, J., et al., *Coupled particulate and continuum model for nanoparticle targeted delivery.* Computers & Structures, 2013. **122**(0): p. 128-134.

68. Sohrabi, S., et al., *Numerical Simulation of Particle Transport and Deposition in the Pulmonary Vasculature.* Journal of biomechanical engineering, 2014. **136**(12): p. 121010.

69. Twombly, R., *Cancer surpasses heart disease as leading cause of death for all but the very elderly.* Journal of the National Cancer Institute, 2005. **97**(5): p. 330-331.

70. Pantel, K. and C. Alix-Panabières, *Circulating tumour cells in cancer patients: challenges and perspectives.* Trends in molecular medicine, 2010. **16**(9): p. 398-406.

71. Gascoyne, P.R., et al., *Isolation of rare cells from cell mixtures by dielectrophoresis.* Electrophoresis, 2009. **30**(8): p. 1388-1398.

72. Hoshino, K., et al., *Microchip-based immunomagnetic detection of circulating tumor cells.* Lab on a Chip, 2011. **11**(20): p. 3449-3457.

73. Wang, M.M., et al., *Microfluidic sorting of mammalian cells by optical force switching.* Nature biotechnology, 2005. **23**(1): p. 83-87.

74. Didar, T.F. and M. Tabrizian, *Adhesion based detection, sorting and enrichment of cells in microfluidic Lab-on-Chip devices.* Lab on a Chip, 2010. **10**(22): p. 3043-3053.

75. Wang, G., et al., *Stiffness dependent separation of cells in a microfluidic device.* PLoS One, 2013. **8**(10): p. e75901.

76. Eisenstein, M., *Cell sorting: divide and conquer.* Nature, 2006. **441**(7097): p. 1179-1185.

77. Wang, S., et al., *Geometry design of herringbone structures for cancer cell capture in a microfluidic device.* Microfluidics and Nanofluidics, 2016. **20**(11): p. 148.

78. Pommer, M.S., et al., *Dielectrophoretic separation of platelets from diluted whole blood in microfluidic channels.* Electrophoresis, 2008. **29**(6): p. 1213-1218.

79. Doh, I. and Y.-H. Cho, *A continuous cell separation chip using hydrodynamic dielectrophoresis (DEP) process.* Sensors and Actuators A: Physical, 2005. **121**(1): p. 59-65.

80. Pamme, N. and C. Wilhelm, *Continuous sorting of magnetic cells via on-chip free-flow magnetophoresis.* Lab on a Chip, 2006. **6**(8): p. 974-980.

81. Xia, N., et al., *Combined microfluidic-micromagnetic separation of living cells in continuous flow.* Biomedical Microdevices, 2006. **8**(4): p. 299-308.

82. Petersson, F., et al., *Free flow acoustophoresis: microfluidic-based mode of particle and cell separation.* Analytical chemistry, 2007. **79**(14): p. 5117-5123.

83. Shi, J., et al., *Continuous particle separation in a microfluidic channel via standing surface acoustic waves (SSAW).* Lab on a Chip, 2009. **9**(23): p. 3354-3359.

84. Ekpenyong, A.E., et al., *Viscoelastic properties of differentiating blood cells are fate-and function-dependent.* PLoS One, 2012. **7**(9): p. e45237.

85. Ren, L., et al., *A high-throughput acoustic cell sorter.* Lab on a Chip, 2015. **15**(19): p. 3870-3879.

86. Yunus, D.E., et al., *Acoustic patterning for 3D embedded electrically conductive wire in stereolithography.* Journal of Micromechanics and Microengineering, 2017. **27**(4): p. 045016.

87. Nawaz, A.A., et al., *Acoustofluidic Fluorescence Activated Cell Sorter.* Analytical chemistry, 2015. **87**(24): p. 12051-12058.

88. Takahashi, K., et al., *Non-destructive on-chip cell sorting system with real-time microscopic image processing.* Journal of nanobiotechnology, 2004. **2**(1): p. 5.

89. Fu, A.Y., et al., *An integrated microfabricated cell sorter.* Analytical Chemistry, 2002. **74**(11): p. 2451-2457.

90. Di Carlo, D., et al., *Continuous inertial focusing, ordering, and separation of particles in microchannels.* Proceedings of the National Academy of Sciences, 2007. **104**(48): p. 18892-18897.

91. Huang, L.R., et al., *Continuous particle separation through deterministic lateral displacement.* Science, 2004. **304**(5673): p. 987-990.

92. Yamada, M. and M. Seki, *Hydrodynamic filtration for on-chip particle concentration and classification utilizing microfluidics.* Lab on a Chip, 2005. **5**(11): p. 1233-1239.

93. Xu, W., et al., *Cell stiffness is a biomarker of the metastatic potential of ovarian cancer cells.* PloS one, 2012. **7**(10): p. e46609.

94. Lincoln, B., et al., *Deformability - based flow cytometry.* Cytometry Part A, 2004. **59**(2): p. 203-209.

95. Hur, S.C., et al., *Deformability-based cell classification and enrichment using inertial microfluidics.* Lab on a Chip, 2011. **11**(5): p. 912-920.

96. Shimeta, J. and M. Koehl, *Mechanisms of particle selection by tentaculate suspension feeders during encounter, retention, and handling.* Journal of Experimental Marine Biology and Ecology, 1997. **209**(1): p. 47-73.

97. Fox, R., *Invertebrate zoology*. 2001: Wadsworth Publishing.

98. Enuka, Y., et al., *Epithelial sodium channels (ENaC) are uniformly distributed on motile cilia in the oviduct and the respiratory airways.* Histochemistry and cell biology, 2012. **137**(3): p. 339-353.

99. den Toonder, J.M. and P.R. Onck, *Microfluidic manipulation with artificial/bioinspired cilia.* Trends in biotechnology, 2013. **31**(2): p. 85-91.

100. Mukhopadhyay, R., *When microfluidic devices go bad.* Analytical chemistry, 2005. **77**(21): p. 429 A-432 A.

101. den Toonder, J., et al., *Artificial cilia for active micro-fluidic mixing.* Lab on a Chip, 2008. **8**(4): p. 533-541.

102. Shields, A., et al., *Biomimetic cilia arrays generate simultaneous pumping and mixing regimes.* Proceedings of the National Academy of Sciences, 2010. **107**(36): p. 15670-15675.

103. Oh, K., et al., *Characterization of mixing performance for bio-mimetic silicone cilia.* Microfluidics and nanofluidics, 2010. **9**(4-5): p. 645-655.

104. Pokroy, B., et al., *Fabrication of bioinspired actuated nanostructures with arbitrary geometry and stiffness.* Advanced Materials, 2009. **21**(4): p. 463-469.

105. Ghosh, R., et al., *Designing oscillating cilia that capture or release microscopic particles.* Langmuir, 2009. **26**(4): p. 2963-2968.

106. Bhattacharya, A., et al., *Propulsion and trapping of microparticles by active cilia arrays.* Langmuir, 2012. **28**(6): p. 3217-3226.

107. Bhattacharya, A. and A.C. Balazs, *Stiffness-modulated motion of soft microscopic particles over active adhesive cilia.* Soft Matter, 2013. **9**(15): p. 3945-3955.

108. Ballard, M., et al., *Enhancing nanoparticle deposition using actuated synthetic cilia.* Microfluidics and nanofluidics, 2014. **17**(2): p. 317-324.

109. Shum, H., et al., *Active Ciliated Surfaces Expel Model Swimmers.* Langmuir, 2013. **29**(41): p. 12770-12776.

110. Tripathi, A., A. Bhattacharya, and A.C. Balazs, *Size selectivity in artificial cilia–particle interactions: mimicking the behavior of suspension feeders.* Langmuir, 2013. **29**(14): p. 4616-4621.

111. Branscomb, J. and A. Alexeev, *Designing ciliated surfaces that regulate deposition of solid particles.* Soft Matter, 2010. **6**(17): p. 4066-4069.

112. Tripathi, A., H. Shum, and A.C. Balazs, *Fluid-driven motion of passive cilia enables the layer to expel sticky particles.* Soft matter, 2014. **10**(9): p. 1416-1427.

113. Balazs, A.C., et al., *Designing Bioinspired Artificial Cilia to Regulate Particle–Surface Interactions.* The journal of physical chemistry letters, 2014. **5**(10): p. 1691-1700.

114. He, X., S. Chen, and R. Zhang, *A lattice Boltzmann scheme for incompressible multiphase flow and its application in simulation of Rayleigh–Taylor instability.* Journal of Computational Physics, 1999. **152**(2): p. 642-663.

115. He, X., S. Chen, and G.D. Doolen, *A novel thermal model for the lattice Boltzmann method in incompressible limit.* Journal of Computational Physics, 1998. **146**(1): p. 282-300.

116. Yuan, P. and L. Schaefer, *Equations of state in a lattice Boltzmann model.* Physics of Fluids, 2006. **18**(4): p. 042101.

117. Chen, S. and G.D. Doolen, *LATTICE BOLTZMANN METHOD FOR FLUID FLOWS.* Annual Review of Fluid Mechanics, 1998. **30**(1): p. 329-364.

118. Luo, L.S., *THE LATTICE-GAS AND LATTICE BOLTZMANN METHODS:PAST, PRESENT, AND FUTURE.* International Conference on Applied Computational Fluid Dynamics, 2000: p. 52-83.

119. Succi, S., *The Lattice Boltzmann Equation for Fluid Dynamics and Beyond, Clarendon*. 2001, Oxford.

120. Latt, J., *Hydrodynamic limit of lattice Boltzmann equations*. 2007, University of Geneva.

121. Qian, Y., D. d'Humières, and P. Lallemand, *Lattice BGK models for Navier-Stokes equation.* EPL (Europhysics Letters), 1992. **17**(6): p. 479.

122. Gong, S. and P. Cheng, *Numerical investigation of droplet motion and coalescence by an improved lattice Boltzmann model for phase transitions and multiphase flows.* Computers & Fluids, 2012. **53**: p. 93-104.

123. Hecht, M. and J. Harting, *Implementation of on-site velocity boundary conditions for D3Q19 lattice Boltzmann simulations.* Journal of Statistical Mechanics: Theory and Experiment, 2010. **2010**(01): p. P01018.

124. Li, J., et al., *Cytoskeletal dynamics of human erythrocyte.* Proceedings Of the National Academy Of Sciences Of the United States Of America, 2007. **104**(12): p. 4937-4942.

125. Li, H. and G. Lykotrafitis, *Two-component coarse-grained molecular-dynamics model for the human erythrocyte membrane.* Biophysical journal, 2012. **102**(1): p. 75-84.

126. Dao, M., J. Li, and S. Suresh, *Molecularly based analysis of deformation of spectrin network and human erythrocyte.* Materials Science & Engineering C-Biomimetic and Supramolecular Systems, 2006. **26**(8): p. 1232-1244.

127. Fedosov, D.A., et al., *Multiscale Modeling of Red Blood Cell Mechanics and Blood Flow in Malaria.* Plos Computational Biology, 2011. **7**(12).

128. Nakamura, M., S. Bessho, and S. Wada, *Spring-network-based model of a red blood cell for simulating mesoscopic blood flow.* International Journal for Numerical Methods in Biomedical Engineering, 2013. **29**(1): p. 114-128.

129. Dao, M., J. Li, and S. Suresh, *Molecularly based analysis of deformation of spectrin network and human erythrocyte.* Materials Science and Engineering: C, 2006. **26**(8): p. 1232-1244.

130. Buxton, G.A., C.M. Care, and D.J. Cleaver, *A lattice spring model of heterogeneous materials with plasticity.* Modelling and simulation in materials science and engineering, 2001. **9**(6): p. 485.

131. Mills, J., et al., *Nonlinear elastic and viscoelastic deformation of the human red blood cell with optical tweezers.* MCB-TECH SCIENCE PRESS-, 2004. **1**: p. 169-180.

132. Fedosov, D., B. Caswell, and G.E. Karniadakis. *Coarse-grained red blood cell model with accurate mechanical properties, rheology and dynamics*. in *Engineering in Medicine and Biology Society, 2009. EMBC 2009. Annual International Conference of the IEEE*. 2009. IEEE.

133. Pivkin, I.V. and G.E. Karniadakis, *Accurate coarse-grained modeling of red blood cells.* Physical review letters, 2008. **101**(11): p. 118105.

134. Schmid-Schönbein, H., P. Gaehtgens, and H. Hirsch, *On the shear rate dependence of red cell aggregation in vitro.* Journal of Clinical Investigation, 1968. **47**(6): p. 1447.

135. Down, L.A., D.V. Papavassiliou, and A. Edgar, *Significance of extensional stresses to red blood cell lysis in a shearing flow.* Annals of biomedical engineering, 2011. **39**(6): p. 1632-1642.

136. Leverett, L., et al., *Red blood cell damage by shear stress.* Biophysical journal, 1972. **12**(3): p. 257.

137. Abkarian, M., M. Faivre, and A. Viallat, *Swinging of red blood cells under shear flow.* Physical review letters, 2007. **98**(18): p. 188302.

138. Fischer, T.M., *Tank-tread frequency of the red cell membrane: dependence on the viscosity of the suspending medium.* Biophysical journal, 2007. **93**(7): p. 2553-2561.

139. Wexler, J.S., et al., *Bending of elastic fibres in viscous flows: the influence of confinement.* Journal of fluid mechanics, 2013. **720**: p. 517-544.

140. Clausen, J.R., D.A. Reasor, and C.K. Aidun, *Parallel performance of a lattice-Boltzmann/finite element cellular blood flow solver on the IBM Blue Gene/P architecture.* Computer physics communications, 2010. **181**(6): p. 1013-1020.

141. Tomasini, M.D., C. Rinaldi, and M.S. Tomassone, *Molecular dynamics simulations of rupture in lipid bilayers.* Experimental Biology and Medicine, 2010. **235**(2): p. 181-188.

142. Li, H. and G. Lykotrafitis, *A coarse-grain molecular dynamics model for sickle hemoglobin fibers.* Journal Of the Mechanical Behavior Of Biomedical Materials, 2011. **4**(2): p. 162-173.

143. Mills, Z.G., W. Mao, and A. Alexeev, *Mesoscale modeling: solving complex flows in biology and biotechnology.* Trends in Biotechnology, 2013. **31**(7): p. 426-434.

144. Li, X.J., B. Caswell, and G.E. Karniadakis, *Effect of Chain Chirality on the Self-Assembly of Sickle Hemoglobin.* Biophysical Journal, 2012. **103**(6): p. 1130-1140.

145. Thomas, A., et al., *Characterization of vascular permeability using a biomimetic microfluidic blood vessel model.* Biomicrofluidics, 2017. **11**(2): p. 024102.

146. Hallow, D.M., et al., *Shear‐induced intracellular loading of cells with molecules by controlled microfluidics.* Biotechnology and bioengineering, 2008. **99**(4): p. 846-854.

147. Chang, D. and T.S. Reese, *Changes in membrane structure induced by electroporation as revealed by rapid-freezing electron microscopy.* Biophysical Journal, 1990. **58**(1): p. 1.

148. Tolpekina, T., W. Den Otter, and W. Briels, *Simulations of stable pores in membranes: system size dependence and line tension.* The Journal of chemical physics, 2004. **121**(16): p. 8014-8020.

149. den Otter, W.K., *Free energies of stable and metastable pores in lipid membranes under tension.* The Journal of chemical physics, 2009. **131**(20): p. 205101.

150. Leontiadou, H., A.E. Mark, and S.J. Marrink, *Molecular dynamics simulations of hydrophilic pores in lipid bilayers.* Biophysical journal, 2004. **86**(4): p. 2156-2164.

151. Erickson, H.P., *Size and shape of protein molecules at the nanometer level determined by sedimentation, gel filtration, and electron microscopy.* Biol Proced Online, 2009. **11**(1): p. 32-51.

152. Doster, W. and S. Longeville, *Microscopic diffusion and hydrodynamic interactions of hemoglobin in red blood cells.* Biophysical journal, 2007. **93**(4): p. 1360-1368.

153. Riveros-Moreno, V. and J.B. Wittenberg, *The self-diffusion coefficients of myoglobin and hemoglobin in concentrated solutions.* Journal of Biological Chemistry, 1972. **247**(3): p. 895-901.

154. Davidson, M.G. and W.M. Deen, *Hydrodynamic theory for the hindered transport of flexible macromolecules in porous membranes.* Journal of membrane science, 1988. **35**(2): p. 167-192.

155. Sohrabi, S., et al., *Three-dimensional simulation of urine concentrating mechanism in a functional unit of rat outer medulla. I. Model structure and base case results.* Mathematical biosciences, 2014. **258**: p. 44-56.

156. Davidson, M.G. and W.M. Deen, *Hindered diffusion of water-soluble macromolecules in membranes.* Macromolecules, 1988. **21**(12): p. 3474-3481.

157. Casassa, E.F., *Equilibrium distribution of flexible polymer chains between a macroscopic solution phase and small voids.* Journal of Polymer Science Part B: Polymer Letters, 1967. **5**(9): p. 773-778.

158. Heuser, G. and R. Opitz, *A Couette viscometer for short time shearing of blood.* Biorheology, 1979. **17**(1-2): p. 17-24.

159. Alexeev, A., J. Yeomans, and A.C. Balazs, *Designing synthetic, pumping cilia that switch the flow direction in microchannels.* Langmuir, 2008. **24**(21): p. 12102-12106.

160. Alexeev, A., et al. *Using Actuated Cilia to Regulate Motion of Microscopic Particles*. in *ASME 2010 First Global Congress on NanoEngineering for Medicine and Biology*. 2010. American Society of Mechanical Engineers.

161. Evans, E. and Y.-C. Fung, *Improved measurements of the erythrocyte geometry.* Microvascular Research, 1972. **4**(4): p. 335-347.

162. Lekka, M., et al., *Elasticity of normal and cancerous human bladder cells studied by scanning force microscopy.* European Biophysics Journal, 1999. **28**(4): p. 312-316.

163. Byun, S., et al., *Characterizing deformability and surface friction of cancer cells.* Proceedings of the National Academy of Sciences, 2013. **110**(19): p. 7580-7585.

164. Fedosov, D.A., J. Fornleitner, and G. Gompper, *Margination of white blood cells in microcapillary flow.* Physical review letters, 2012. **108**(2): p. 028104.

165. Pries, A., D. Neuhaus, and P. Gaehtgens, *Blood viscosity in tube flow: dependence on diameter and hematocrit.* American Journal of Physiology-Heart and Circulatory Physiology, 1992. **263**(6): p. H1770-H1778.

166. Hsu, C.-H., et al., *Microvortex for focusing, guiding and sorting of particles.* Lab on a Chip, 2008. **8**(12): p. 2128-2134.

167. Zou, Q.S. and X.Y. He, *On pressure and velocity boundary conditions for the lattice Boltzmann BGK model.* Physics of Fluids, 1997. **9**(6): p. 1591-1598.

168. Handelman, G.J. and N.W. Levin, *Red cell survival: relevance and mechanism involved.* Journal of Renal Nutrition, 2010. **20**(5): p. S84-S88.

169. Januszewski, M. and M. Kostur, *Sailfish: A flexible multi-GPU implementation of the lattice Boltzmann method.* Computer Physics Communications, 2014. **185**(9): p. 2350-2368.

170. Latt, J., *Palabos, parallel lattice Boltzmann solver*. 2009.

171. Schumacher, J.T., et al., *System development for generating homogeneous cell suspensions and transporting them in microfluidic devices.* Engineering In Life Sciences, 2008. **8**(1): p. 49-55.

172. Nair, K., et al., *Characterization of cell viability during bioprinting processes.* Biotechnology journal, 2009. **4**(8): p. 1168-1177.

173. Lorber, B., et al., *Adult rat retinal ganglion cells and glia can be printed by piezoelectric inkjet printing.* Biofabrication, 2014. **6**(1): p. 015001.

174. Ang, T.H., et al., *Fabrication of 3D chitosan–hydroxyapatite scaffolds using a robotic dispensing system.* Materials Science and Engineering: C, 2002. **20**(1–2): p. 35-42.

175. Boland, T., et al., *Cell and organ printing 2: Fusion of cell aggregates in three-dimensional gels.* The Anatomical Record Part A: Discoveries in Molecular, Cellular, and Evolutionary Biology, 2003. **272A**(2): p. 497-502.

176. Lokanathan, A.R., et al., *Cilia-Mimetic hairy surfaces based on end-immobilized nanocellulose colloidal rods.* Biomacromolecules, 2013. **14**(8): p. 2807-2813.

177. Wang, Y., et al., *Out of the cleanroom, self-assembled magnetic artificial cilia.* Lab on a Chip, 2013. **13**(17): p. 3360-3366.

178. Hussong, J., et al., *Experimental investigation of the flow induced by artificial cilia.* Lab on a Chip, 2011. **11**(12): p. 2017-2022.

179. Zhou, B., et al., *Design and fabrication of magnetically functionalized flexible micropillar arrays for rapid and controllable microfluidic mixing.* Lab on a Chip, 2015. **15**(9): p. 2125-2132.

180. Chen, C.-Y., et al., *Magnetically actuated artificial cilia for optimum mixing performance in microfluidics.* Lab on a Chip, 2013. **13**(14): p. 2834-2839.

181. Evans, B., et al., *Magnetically actuated nanorod arrays as biomimetic cilia.* Nano letters, 2007. **7**(5): p. 1428-1434.

182. Moraes, C., et al., *Supersoft lithography: candy-based fabrication of soft silicone microstructures.* Lab on a Chip, 2015. **15**(18): p. 3760-3765.

183. Liu, F., et al., *An inverted micro-mixer based on a magnetically-actuated cilium made of Fe doped PDMS.* Smart Materials and Structures, 2016. **25**(9): p. 095049.

184. He, R., et al., *Generation of customizable micro-wavy pattern through grayscale direct image lithography.* Scientific reports, 2016. **6**.

185. He, R., et al., *Fabrication of circular microfluidic channels through grayscale dual-projection lithography.* Microfluidics and Nanofluidics, 2017. **21**(1): p. 13.

Appendix

Vita

Salman Sohrabi was born on August, 30, 1988 at Tehran, Iran. He is the son of Khadijeh Tadayon and AliAkbar Sohrabi. He received his Bachelor Degree in Mechanical Engineering in 2010 and Master Degree in Mechanical engineering from Sharif University of Technology in 2012. He has 17 published papers and 2 submitted papers. He is a Rossin Doctor Fellow in Lehigh University. He also acquired a lot of teaching experience through serving as teacher assistant in Lehigh University.